RESEARCH ARTICLE

Identifying Site-Specific Superoxide and Hydrogen Peroxide Production Rates From the Mitochondrial Electron Transport System Using a Computational Strategy

Quynh V. Duong[1], Yan Levitsky[2], Maria J. Dessinger[2], Jasiel O. Strubbe-Rivera[3], Jason N. Bazil [2,*]

[1]Department of Biochemistry and Molecular Biology, Michigan State University, East Lansing, Michigan 48824, USA, [2]Department of Physiology, Michigan State University, East Lansing, Michigan 48824, USA and [3]Department of Pharmacology and Toxicology, Michigan State University, East Lansing, Michigan 48824, USA
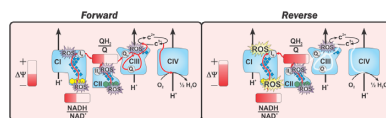
*Address correspondence to J.N.B. (e-mail: jnbazil@msu.edu)

Abstract

Mitochondrial reactive oxygen species (ROS) play important roles in cellular signaling; however, certain pathological conditions such as ischemia/reperfusion (I/R) injury disrupt ROS homeostasis and contribute to cell death. A major impediment to developing therapeutic measures against oxidative stress-induced cellular damage is the lack of a quantitative framework to identify the specific sources and regulatory mechanisms of mitochondrial ROS production. We developed a thermodynamically consistent, mass-and-charge balanced, kinetic model of mitochondrial ROS homeostasis focused on redox sites of electron transport chain complexes I, II, and III. The model was calibrated and corroborated using comprehensive data sets relevant to ROS homeostasis. The model predicts that complex I ROS production dominates other sources under conditions favoring a high membrane potential with elevated nicotinamide adenine dinucleotide (NADH) and ubiquinol (QH_2) levels. In general, complex I contributes to significant levels of ROS production under pathological conditions, while complexes II and III are responsible for basal levels of ROS production, especially when QH_2 levels are elevated. The model also reveals that hydrogen peroxide production by complex I underlies the non-linear relationship between ROS emission and O_2 at low O_2 concentrations. Lastly, the model highlights the need to quantify scavenging system activity under different conditions to establish a complete picture of mitochondrial ROS homeostasis. In summary, we describe the individual contributions of the electron transport system complex redox sites to total ROS emission in mitochondria respiring under various combinations of NADH- and Q-linked respiratory fuels under varying workloads.

Introduction

Reactive oxygen species (ROS) are by-products of cellular respiration, but they are now recognized as important signaling molecules.[1–4] Under pathological conditions such as ischemia/reperfusion (I/R) injury, elevated ROS levels contribute to cell death.[5] This type of injury occurs after a period of partial or complete loss of tissue blood flow (ischemia) followed by the restoration of normal flow (reperfusion). Although reperfusion is necessary to salvage ischemic tissue, it leads to significant tissue damage in a ROS-dependent manner.[5] This unfortunate and common event is also associated with clinical situations such as organ transplantation[6] and hypovolemic shock.[7] Though I/R injury can affect any organ, metabolically active tissue such as brain and myocardium are the most sensitive to this injury. Despite enormous efforts to ameliorate the detrimental effects of reperfusion-dependent oxidative stress, pharmacological interventions have not produced effective clinical treatment options.[5,8,9] A more complete understanding of redox site-specific ROS emission in I/R injury may lead to the design of efficient pharmacologic interventions.

In most mammalian cells, mitochondria are the primary source of ROS.[10–12] As such, mitochondrial ROS homeostasis is essential to maintaining mitochondrial and cellular physiology. In essence, ROS production and elimination act as countering forces which determine the mitochondrial net ROS emission. The mechanisms underlying ROS production have been reviewed extensively elsewhere,[13,14] and only key details are provided here. The electron transport system (ETS) complexes I and III are accepted as the major mitochondrial ROS producers; however, their respective contributions to total ROS emission vary according to the bioenergetic state of the organelle.[10] Matrix and non-ETS inner membrane proteins can also produce ROS, but their contribution is limited.[15–17] Under physiological conditions, electron flux through the ETS favors forward electron transport (FET). In this operating mode, pyruvate (P) from glucose metabolism is oxidized through the Krebs cycle to generate nicotinamide adenine dinucleotide (NADH), which enters the ETS at complex I. When succinate (S) is oxidized, electrons enter the ETS at complex II. Despite the different entry points, electrons converge at the quinone (Q) pool before they are passed onto cytochrome c and ultimately molecular oxygen (O_2). This is the normal flow of electrons during energy transduction. During certain pathological states, ETS circuitry is rewired due to a change in substrate availability. For example, during anoxia, the forward electron flow through complex I is supported by reversal of complex II while the activities of complexes III and IV dramatically fall near zero.[18,19] Reorganization of electron flux causes succinate and ubiquinol (QH_2) to accumulate as fumarate reduction at complex II replaces O_2 reduction at complex IV. Upon reperfusion, O_2 is reintroduced into the system, and electron flow normalizes. With high levels of QH_2, thermodynamic and kinetic processes favor ETS operation in the reverse electron transport (RET) mode. In this mode, complex I enters a near equilibrium state with nearly all its redox centers fully reduced

and produces ROS at significantly elevated rates. Thus, ROS production is enhanced under RET compared to FET with the former playing a significant role in I/R-induced oxidative stress.

The majority of O_2 is fully reduced to water at complex IV; however, one- or two-electron reduction of O_2 by an ETS redox center upstream of complex IV produces superoxide or hydrogen peroxide, respectively. In complex I, the redox centers include a flavin mononucleotide (FMN) at the NADH oxidase site (site I_F),[20] a semiquinone (SQ) at the Q reductase site (site I_Q)[21] and a chain of iron-sulfur (Fe-S) clusters that rapidly relay electrons between the two.[22,23] Likewise, complex II harbors a flavin adenine dinucleotide (FAD) at the succinate oxidase site (II_F), a Q reductase site (II_Q), and a chain of Fe-S clusters.[24,25] The mammalian complex III redox centers include cytochrome c_1, a high- and low-potential b type heme, the Rieske iron-sulfur protein (ISP), and two quinone binding sites (Q_N and Q_P).[26] Superoxide arising from complex III is generally accepted to originate from the SQ at the quinone binding site proximal to the intermembrane space (Q_P).[27]

The topic of site-specific ROS production has attracted experimental researchers for many years. Both pharmacological and genetic approaches have been utilized to dissect the contribution of redox centers to total mitochondrial ROS. While complexes I and III are the major ROS producers, the contribution of specific redox centers at physiologically relevant metabolic states remains elusive. For example, both site I_F[28–30] and I_Q[31] are proposed as major ROS-producing sites of complex I. Complex II was widely accepted as a negligible source of ETS ROS.[32] However, several more recent studies report that complex II produces significant amounts of ROS under appropriate conditions.[33,34] Such discrepancies in experimental data arise from the caveats inherent to experimental studies and have contributed to unsuccessful efforts to target oxidative stress in clinical settings. In particular, the use of chemical inhibitors and genetic models inevitably alter the native electron distribution in unpredictable patterns, leading to epiphenomena and conflicting experimental results. Differences in experimental conditions including species, tissues, developmental stage, etc. introduce additional confounding factors that are often neglected and make comparing results from different studies difficult. Lastly, the pursuit is further impeded by the lack of a robust method to distinguish species-specific ROS without interfering with other mitochondrial and extra-mitochondrial processes.

Computational modeling is a useful platform to address these challenges. A computational model serves as a quantitative framework to analyze mitochondrial bioenergetic data from a single, unified perspective. Several models of mitochondria exist at varying levels of complexity, focus, and approach.[35–42] Some investigate the kinetics underlying ROS production by individual ETS complexes[38–40,43–45] while others integrate mitochondrial ROS production and elimination in a substrate-specific context.[41,42,46] However, to our knowledge, none consistently reproduces a wide range of experimental data using a unified, coherent, and consistent framework. Thus, the origin of

superoxide and hydrogen peroxide from the ETS remains elusive from a computational or experimental perspective.

We herein developed, analyzed, and corroborated a comprehensive model that simulates mitochondrial ROS homeostasis under a range of bioenergetic conditions. This model is focused on ROS from the ETS and is referred to as the ETS-ROS model. Modules relevant to ROS originating from the ETS were individually developed, parameterized, and corroborated against a variety of data sets.[38–40] The model includes the primary ROS producers in mitochondria with their biochemical reactions constrained thermodynamically and balanced with respect to mass and charge. These modules were then incorporated into a single integrated framework, producing a model that is coherent and operates within biophysical constraints using a single, consistent set of parameters. The ETS-ROS model reproduces experimental data of not only net ROS production but also other mitochondrial bioenergetic variables. Using this approach, we have identified the regulation of ROS production by substrate metabolism *via* alterations to the mitochondrial membrane potential along with the NAD and Q pool redox states. The model also reveals that the scavenging system is saturable with a K_M for H_2O_2 in the nM range. Therefore, under pathological conditions such as I/R injury, cellular oxidative stress is a result of ROS production overwhelming ROS elimination.

Materials and Methods

Computational Model

General Approach to Modeling and Processes Included
Our modeling approach is modular and contains enzyme kinetic and ROS production models of complexes I,[38] II,[39] and III[40] previously published by our group. These models are biophysically detailed and thermodynamically consistent. They were individually calibrated and corroborated against a wide range of kinetic data sets. In this ETS-ROS model, we opted to explicitly model part of the Krebs cycle while lumping other parts. The explicit parts of the model consist of the enzymatic reactions that support succinate, fumarate, and malate transport and oxidation. Pyruvate transport is explicitly modeled; however, pyruvate dehydrogenase and the upper branch of the Krebs cycle (citrate synthase through succinyl-CoA synthetase) were modeled as a lumped reaction. This lumped reaction was sufficient to explain the experimental data. The detailed reactions for the lumped portion of the model are excluded to stay faithful to the parsimonious principle. In addition, our in-house experimental data reveal a moderate level of malic enzyme (ME) activity in mitochondria isolated from guinea pig ventricular cardiomyocytes (Figure S1). Several other studies also support the expression of ME in cardiac tissue of guinea pigs,[47,48] and we found this reaction necessary to fit the model to the calibration data sets. Other biochemical processes such as spontaneous oxaloacetate decarboxylation[49] may also help explain these data. We will test this and other ideas when the model is updated to include more detailed Krebs cycle reactions. A summary of processes that are explicitly modeled are shown in Figure 1. Notations of the redox centers included in the text are described in Table 1.

Model Simulations
The model was numerically simulated using MATLAB (R2020b). The parameter optimization was performed on a Dell desktop PC (64-bit operating system and x64-based processor Intel® core™ i7-7700 CPU @3.60GHz and 16 GB RAM) using the Parallel Computing Toolbox. A parallelized simulated annealing algorithm was first used to globally search for feasible parameters, which were then refined using a local, gradient-based optimization algorithm. When fitting to the calibration data, the difference between model output and data were normalized with the respetive uncertainty in the data and minimzed using the standard least squares method.

Data Sets
The intricate relationship between substrate utilization and ROS homeostasis necessitates that model calibration includes experimental data describing both NADH- and QH_2-linked substrate supported respiration and ROS production. The calibration data set includes the oxygen consumption rates (J_{O2}, nmol/mg/min), net hydrogen peroxide emission rates (J_{H2O2}, pmol/mg/min) and NADH reduction (%) under NADH- and QH_2-linked supported respiration in both FET and RET modes. FET occurs when respiration is supported by pyruvate/L-malate (P/M) and S in the presence of rotenone (S/R). RET occurs under QH_2-linked supported respiration when rotenone is absent (S). The calibrated model is subsequently challenged against novel data sets, those which were not used for model calibration. The first corroboration data set includes the J_{O2} and J_{H2O2} data obtained when respiration is supported by both NADH- and QH_2-linked substrates (P/M/S). The second data set recapitulates the monotonic relationship of J_{H2O2} on oxygen concentrations in FET mode. The list of all the data sets utilized in the construction, calibration and corroboration of the model is summarized in Table 2.

The majority of the experimental data used for model calibration were from a previous publication of ours.[50] In this study, we measured the oxygen consumption rate (J_{O2}, nmol mg^{-1} min^{-1}) and net hydrogen peroxide emission rate (J_{H2O2}, pmol mg^{-1} min^{-1}) of mitochondria respiring on P/M, S and S/R. Briefly, all experiments were performed using a standard KCl-based mitochondrial suspension buffer containing 130 mM KCl, 5 mM K_2HPO_4, 20 mM MOPS, 1 mM $MgCl_2$, 1 mM EGTA, and 0.1% w/v BSA (pH of 7.1 at 37 °C). For general methods and protocols regarding mitochondrial isolation and bioenergetic experiments, see our prior works.[50,51] When used, the final concentrations of mitochondria, substrates, and inhibitors were 0.1 mg/mL mitochondria, 5 mM pyruvate (P), 1 mM L-malate (M), 10 mM succinate (S), 1 μM rotenone (R), and 500 μM adenosine diphosphate (ADP). The data were analyzed using the software MATLAB®.

Model Parameters
The fixed model parameters are obtained from thermodynamic and kinetic data obtained from prior work.[18,38–40] The adjustable parameter set consists of 14 parameters related to both ROS kinetics and substrate metabolism. We chose the smallest set of adjustable parameters necessary to simulate the calibration data sets. The ROS kinetic parameters are related to mitochondrial production and clearance of superoxide and hydrogen peroxide. The capacity of mitochondria to remove hydrogen peroxide is interchangeably referred to as the scavenging capacity in this paper. The scavenging system is modeled in a Michaelis–Menten like fashion—saturable and dependent on the hydrogen peroxide concentration. The ETS parameters include the enzyme contents for complex I, II, and III, the estimation of the semiquinone stability constant in complex III, and the apparent rotenone binding constant to complex I. The remaining adjustable parameters are concerned with metabolite transport and substrate utilization (Table 3). Normalized local sen-
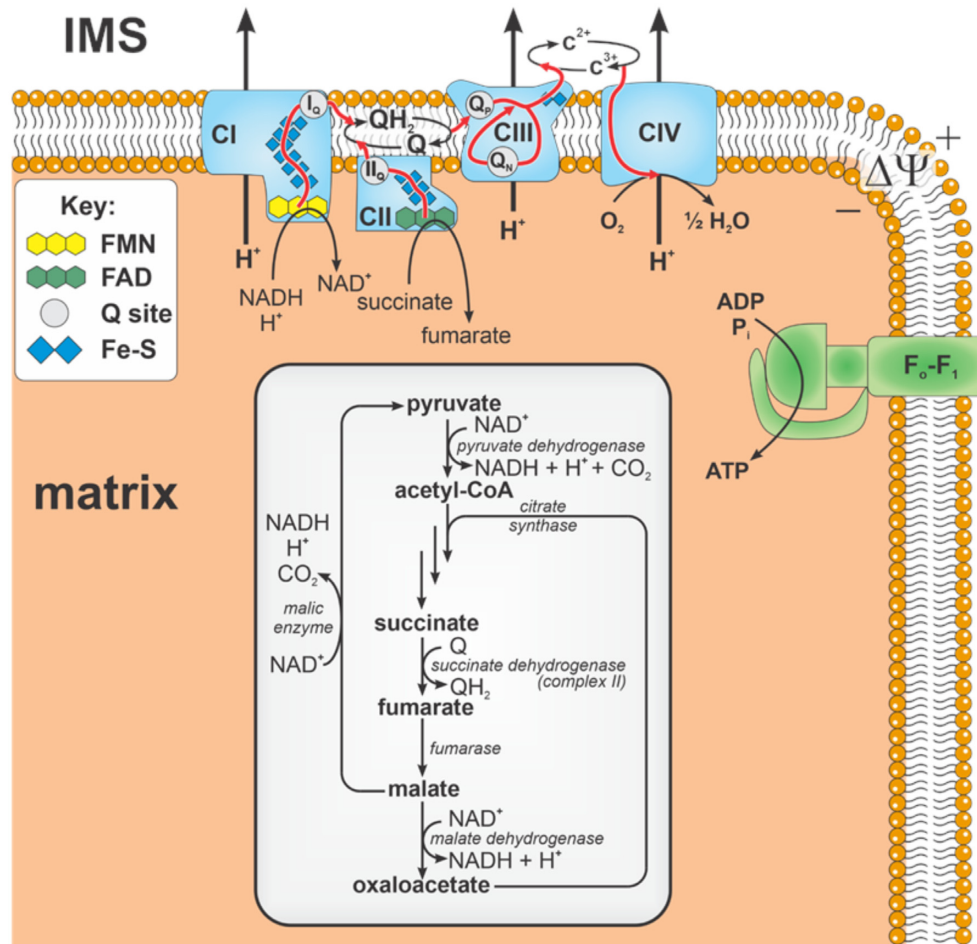
Figure 1. Schematic of modeled biochemical reactions and phenomena. The model consists of a partially lumped Kreb's cycle with non-lumped enzymatic reactions shown in the light gray box. Black arrows denote chemical reactions. Red arrows denote electron flux through redox centers. FMN = flavin mononucleotide, FAD = flavin adenine dinucleotide, Q = ubiquinone, QH_2 = ubiquinol, Fe-S = iron sulfur clusters, IMS = intermembrane space, CI—CIV = complexes I—IV, c = cytochrome c, Q site = quinol/quinone binding site.

Table 1. Description of the ETS Redox Centers Included in the Model

Notations	Description	Species formed
I_Q	Quinone reductase site in complex I	Superoxide
I_{FMNH2}	Fully reduced flavin in complex I	Superoxide, hydrogen peroxide
I_{FMNH}	semiflavin radical in complex I	Superoxide
$II_{[3Fe-4S]}$	[3Fe-4S] cluster in complex II	Superoxide
II_{FADH2}	Fully reduced flavin in complex II	Hydrogen peroxide
II_{FADH}	Semiflavin radical in complex II	Superoxide
III_{Qp}	Q_p site in complex III	Superoxide

For details regarding the approximate location of each site on the complexes, see Figure 1. Site locations are not 100% accurate and drawn for clarity. Subscript indicates the form of the redox cofactor responsible for ROS production. In complex II, site [3Fe-4S] is located at the quinone binding site and thus referred to as II_Q in Figure 1.

sitivity coefficients are computed to inform the contribution of each adjustable parameter to the model output in a similar manner previously described.[38–40] For details on how the analysis was performed, see Section 3 of the supplement. These values are calculated from model outputs coincident with the data and associated dynamics. The sensitivity analysis reveals that the complex I content is the most sensitive parameter followed by complex III content and the H_2O_2 affinity of the matrix scavenging system. These results are not unexpected considering the tight association between respiratory state and ROS emission.

Experimental Methods

Isolated Mitochondria Preparation

We supplemented prior data of ours[50] with additional data to further challenge the model. For these studies, we used Hartley guinea pigs weighing between 350 and 450 g (4–6 wk). Animal care and handling conformed to the National Institutes of Health's Guild for the Care and Use of Laboratory Animals and was approved by Michigan State University's Institutional Animal Care and Use Committee. Isolated mitochondria were isolated from ventricular cardiomyocytes as described in our prior

Table 2. Summary of Data Used in This Study.

Modeling stage	Data sets	References
Calibration	J_{O_2}–P/M, S/R	This study
	J_{O_2}–S	Duong et al.[50]
	$J_{H_2O_2}$–P/M, S/R	This study
	$J_{H_2O_2}$–S	Duong et al.[50]
	$J_{H_2O_2}$ v.s. [O_2]	This study
	J_{O_2}–M	Duong et al.[50]
Corroboration	P/M/S—J_{O_2}, $J_{H_2O_2}$	This study
	NADH—P/M, S/R, S, P/M/S	This study

M: L-malate; P: pyruvate; S: succinate; R: rotenone

work.[51,52] In brief, the guinea pigs were euthanized after being anesthetized with 5% isoflurane and tested to be unresponsive to noxious stimuli. The heart was perfused in chest with ice-cold cardioplegic solution until no blood was observed in the coronary arteries and cardiac veins. The cardioplegic solution consisted of 25 mM KCl, 100 mM NaCl, 10 mM dextrose, 25 mM MOPS, and 1 mM EGTA at pH = 7.15. The heart was then excised and washed with ice-cold isolation buffer consisting of 200 mM mannitol, 50 mM sucrose, 5 mM K_2HPO4, and 0.1% w/v bovine serum albumin (BSA) at pH = 7.15. Ventricular tissue was minced in ice-cold isolation buffer until small pieces remained ($\sim$mm^3). The homogenate was then transferred to a 50 mL canonical tube containing 0.5 U/mL protease (*Bacillus licheniformis*) in 25 mL isolation buffer. A handheld Omni tissue homogenizer was run at 18 000 rpm for 20 sec to liberate mitochondria from cellular components. Mitochondria were then recovered by gradient centrifugation in isolation buffer at 4 °C. Mitochondrial protein was quantified using the bicinchoninic acid assay and BioTek Synergy H1 plate reader. The mitochondrial stock solution was diluted to a working concentration of 40 mg/mL. We routinely run quality control steps to test for mitochondrial quality that include respiratory control ratios (RCRs) (maximum oxphos-state rate/leak-state rate), and we only use mitochondria with control ratios above 16. All reagents were from Sigma unless otherwise noted.

Oxygen Consumption and Net Hydrogen Peroxide Emission Rates
The Oroboros Oxygraph (O2k) was used to simultaneously measure J_{O_2} (nmol mg^{-1} min^{-1}) and $J_{H_2O_2}$ (pmol mg^{-1} min^{-1}), described in detail in our previous publications.[50] Briefly, $J_{H_2O_2}$ values were measured using the Amplex UltraRed/Horseradish Peroxidase/Superoxide Dismutase assay. The reduction of hydrogen peroxide is coupled with the oxidation of Amplex Ultra-Red to resorufin. Resorufin fluorescence is converted to hydrogen peroxide concentration by using a hydrogen peroxide calibration curve obtained each experiment day from freshly prepared hydrogen peroxide standards. A post-hoc analysis of our previous $J_{H_2O_2}$ data sets using S as the substrate reveals that S-dependent $J_{H_2O_2}$ is highly sensitive to the RCR. Higher $J_{H_2O_2}$ values correspond to RCR (energized with P/M and in the presence of 4 μM Ca^{2+}) greater than 18. Thus, we repeated $J_{H_2O_2}$ measurements using mitochondria with an RCR above 18. Mitochondria were energized with L-M, S or the P/M/S combination (leak state). An ADP bolus was added to stimulate oxidative phosphorylation (oxphos state) after 5 min under L-M supported respiration, 2.5 min under S- and 2 min under P/M/S-supported respiration. These time periods were chosen to allow measurement of steady-state J_{O_2} while maintaining adequate oxygen supply for oxidative phosphorylation turnover.

NADH Fluorescence Measurement
The fluorescence of NADH was monitored on an Olis DM-245 spectrofluorometer. Fluorescence was monitored with $\lambda_{excitation}$ = 355 nm (8 nm bandpass filter) and $\lambda_{emission}$ = 450 nm (13 nm bandpass filter). Baseline fluorescence was monitored for 1 min followed by mitochondria addition. Substrates were added after 5 min of equilibration. A bolus of ADP stimulated oxidative phosphorylation. Fluorescence minima were obtained by uncoupling mitochondria with trifluoromethoxy carbonylcyanide phenylhydrazone (FCCP) to produce maximally oxidized nicotinamide pools. Maximal fluorescence was obtained in the presence of rotenone to produce maximally reduced nicotinamide pools.

Results

Model Calibration

The experimental fidelity of the ETS-ROS model is critically related to its ability to predict the in in vivo response of the ETS under a wide variety of physiological and pathophysiological scenarios. Including both FET and RET modes of ROS production data into model calibration was essential to identify the parameters associated with site-specific ROS fluxes under these diverse experimental conditions. In the absence of exogenous ADP, the substrate combinations of P/M and S/R induce FET whereas RET was favored with S as the sole substrate. We used the P/M/S data, which consist of both FET and RET processes, to corroborate the model.

Oxygen Consumption and Net Hydrogen Peroxide Emission Rates
Outputs from the calibrated model were compared to experimentally determined J_{O_2} (nmol/mg/min) and $J_{H_2O_2}$ (pmol/mg/min), as shown in Figure 2 and summarized in Table 4. In general, the model captures the dynamic profile of O_2 consumption as well as H_2O_2 emission rates in a range of energy demand conditions. In the leak state, respiration rates are low and H_2O_2 emission rates are high. This is general for all substrate conditions and is due to membrane polarization and highly reduced mitochondrial redox couples (eg, high NADH/NAD$^+$). When succinate is present, the QH$_2$/Q ratio is large and H_2O_2 emission rates reach even higher values. The highly reduced redox centers in the ETS proteins thermodynamically and kinetically favor elevated ROS emission rates.

When ADP is added, mitochondria enter the oxphos state and dramatically increase their respiratory rate. In this state, redox couples become more oxidized and thus produce ROS at a lower rate compared to leak state. This relationship is also consistent across substrate conditions. Relative to the S/R condition, the absence of rotenone for the S condition did not affect leak-state J_{O_2} but slightly depressed oxphos-state J_{O_2}. This results from NAD pool oxidation leading to oxaloacetate accumulation and complex II inhibition due to malate dehydrogenase turnover.[50,53] Importantly, the H_2O_2 emission rate is dependent on O_2 levels (will be discussed in detail below and briefly here). In these simulations, we modeled the buffer O_2 dynamics as we will show later. Our initial buffer O_2 concentration was 188 μM in a 2 mL volume of uniformly dispersed isolated mitochondria. In our conditions, a respiratory rate of 100 nmol O_2/mg/min corresponds a rate of 10 μM/min which will deplete all the O_2 in 18.8 min. These simulation results show the model not only reproduces the respiratory dynamics associated with various substrates and mitochondrial work rates, but it also simulates

Table 3. Model Adjustable Parameters.

| Parameter	Definition	Value	Unit	Sensitivity	Rank
$Etot_{CI}$	Complex I content	0.167	nmol mg^{-1}	0.118	1
$Etot_{CII}$	Complex II content	0.725	nmol mg^{-1}	0.038	8
$Etot_{CIII}$	Complex III content	0.372	nmol mg^{-1}	0.093	3
V_{max}^{DCC}	Dicarboxylate carrier max transport rate	6860	nmol mg^{-1} min^{-1}	0.007	12
V_{max}^{FH}	Fumarate hydratase max rate	5450	nmol mg^{-1} min^{-1}	0.028	11
X_{DH}	Dehydrogenase activity	7210	nmol mg^{-1} min^{-1}	0.033	10
K_{DH}	Phosphoenergetics feedback constant for matrix dehydrogenase activity	0.124	mM	0.002	13
r_{DH}	NADH/NAD$^+$ feedback constant for matrix dehydrogenase activity	7.60×10^{-3}	–	0.001	14
k_{fME}	Malic enzyme rate constant	3.02×10^6	nmol mg^{-1} min^{-1} M^{-2}	0.043	7
$V_{max}^{scavenge}$	Maximum matrix scavenging rate	31.6	nmol mg^{-1} min^{-1}	0.062	5
$K_M^{scavenge}$	[H$_2$O$_2$] at half maximum scavenging rate	106	nM	0.099	2
$k_{Em,H2O2}$	H$_2$O$_2$ permeability rate constant	5.50×10^5	min^{-1}	0.062	4
K_{CIII}^{SQ}	Complex III semiquinone stability constant	1.40×10^{-12}	–	0.060	6
K_{CI}^{rot}	Complex I rotenone binding constant	1.48	pM	0.037	9
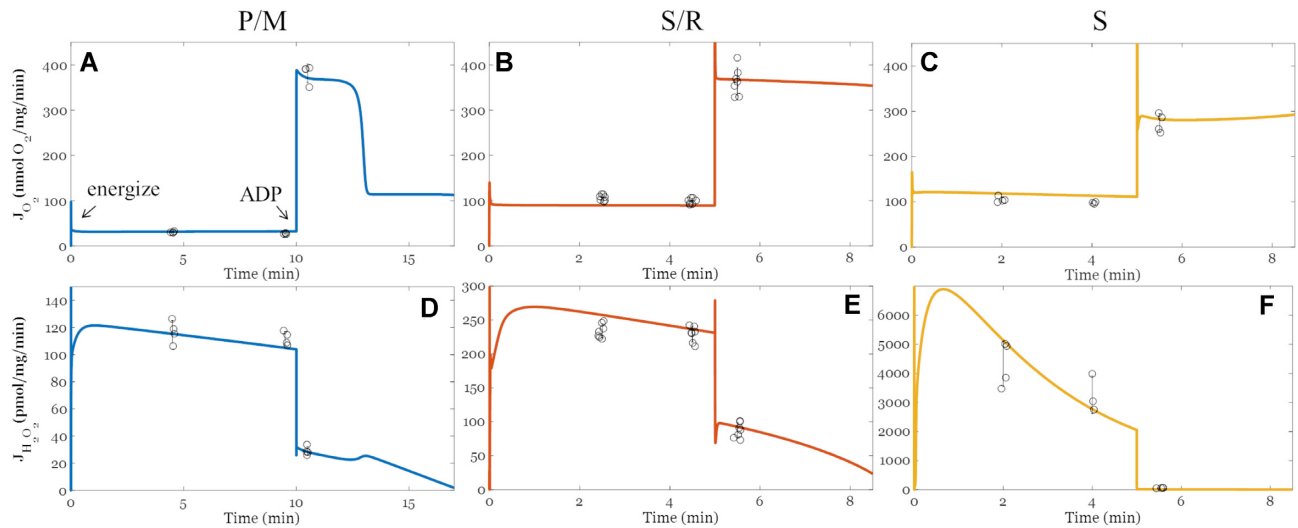
Figure 2. Model simulations of oxygen consumption rates (J_{O2}, nmol/mg/min, *A-C*) and net hydrogen peroxide emission rates (J_{H2O2}, pmol/mg/min, *D-F*) in FET and RET modes. FET occurs when the substrates are P/M (A and D, blue) or S/R (B and E, orange). RET occurs when S is the substrate and rotenone is absent (C and F, yellow). The model outputs are represented by the solid lines. Individual data points are represented by the open black circles; error bars represent the standard deviations. Experimental data are obtained using mitochondria isolated from the ventricular cardiomyocytes of guinea pigs, as described in our previous work.[50] As shown, the model outputs are within the experimental ranges for both J_{O2} and J_{H2O2} in both FET and RET modes.

Table 4. Experimental and Model J_{O2} (nmol/mg/min) and J_{H2O2} (pmol/mg/min).

Substrates	Respiratory state	Experimental J_{O2}	Model J_{O2}	Experimental J_{H2O2}	Model J_{H2O2}
Pyruvate/L-malate (P/M)	5-min leak	30.3 ± 1.4	31	117 ± 8	116
	10-min leak	27 ± 1.1	31	112 ± 5	106
	oxphos	381.4 ± 20.6	377	29 ± 4	29
Succinate/rotenone (S/R)	2.5-min leak	106.4 ± 6.7	89	234 ± 10	259
	5.0-min leak	98.5 ± 6.3	89	229 ± 12	236
	oxphos	363.3 ± 30.6	367	87 ± 11	91
Succinate (S)	2.5-min leak	106.9 ± 8.6	118	4300 ± 775	4995
	5.0-min leak	103.6 ± 4.5	113	3700 ± 991	2707
	oxphos	265.4 ± 36.3	284	61 ± 7	14

free radical emission rates under both FET and RET operating modes.

NADH Reduction States

An essential bioenergetic variable associated with H_2O_2 emission is the NAD redox state. The changes to the NAD^+ pool redox state vary with substrate delivery, ETS flux, and phosphorylation potential, reflecting the overall redox balance of the mitochondrial matrix. As shown in Figure 3, the model is capable of faithfully reproducing experimentally observed NADH dynamics of mitochondria respiring in the leak and oxphos states with P/M or S/R as substrates. Succinate-supported respiration with rotenone yielded a more reduced NADH pool in both leak and oxphos states compared to the P/M substrates. With P/M as the substrates, turnover of NADH at complex I favors a more oxidized NADH pool in leak (80%) and oxphos (30%) states relative to S/R (87.5% and 90%, respectively). The rapid NADH reduction dynamics seen with S/R are a result of residual ME and site I_Q activity. We used 1 μM rotenone in these experiments, and the reported apparent dissociation constant of rotenone binding at the I_Q site is 20 nM.[54] In that study, the I_{50} value was determined using submitochondrial particles with a CoQ_{10} analogue. To properly identify the rotenone dissociation constant, kinetic and free radical studies using intact mitochondria with the native Q molecule used by complex I are necessary. Thus, we opted to fit this parameter with our calibration data sets. The resultant model simulations predict that complex I operates at 2% of its maximum capacity. That said, assuming simple inhibitor kinetics and the above stated I_{50} value for rotenone, residual complex I activity is expected to be ~2% which fits with our model simulations. With the J_{O2}, J_{H2O2}, and now the NADH calibrations, we next sought to challenge our model with an additional substrate combination without adjusting any model parameter other than setting the initial conditions (substrate concentrations).

Model Corroboration

Oxygen Consumption, Net Hydrogen Peroxide Production Rates, and Oxygen Concentration Dynamics Under Both NADH- and QH_2-linked Substrate Metabolism

The final adjustable parameter set (Table 2) was used to simulate the model and predict the J_{O2}, J_{H2O2}, and $[O_2]$ dynamics when mitochondria were energized with a combination of NADH- and QH_2-linked substrates (P/M/S). Under this condition, electrons entering the ETS at complexes I and II converge at the Q pool.[55] Such conditions favor the reduction of the NAD^+ pool, the Q pool, and a high membrane potential, resulting in ROS generation at complex I through RET. As shown in Figure 4, the ETS-ROS model outputs are consistent with experimental data collected from the P/M/S condition. Experimentally determined leak-state J_{O2} (nmol/mg/min) are 129 ± 5 at 2 min and 121 ± 12 at 4 min. The oxphos-state J_{O2} is 729 ± 91 nmol/mg/min. The corresponding simulated J_{O2} (nmol/mg/min) are 116 at 2-min leak state, 114 at 4-min leak state, and 654 during oxphos (Figure 4A). Experimentally measured J_{H2O2} (pmol/mg/min) are 4304 ± 499 at 2-min leak state, 3843 ± 713 at 4-min leak state, and 82 ± 7 during oxphos. The corresponding model predictions are 4449, 3100, and 42 pmol/mg/min (Figure 4B). In general, J_{O2} and J_{H2O2} were significantly elevated compared to the calibration substrate mixtures, which favor electron entry at either complex I or II. With the P/M/S substrate combination, both complex I and complex II are fully engaged to deliver electrons into the Q pool during oxphos. This will increase the respiration rate with

the high substrate delivery favoring reduction of mitochondrial redox couples. The model predicts the resting and active respiratory states with very good accuracy. The small underestimation of ROS emission in the oxphos state is due to minor sources we did not include in this model.

Monotonic Relationship Between J_{H2O2} on $[O_2]$

Although J_{O2} is essentially independent of $[O_2]$ until it drops below 1 μM, the monotonic relationship between J_{H2O2} and $[O_2]$ has been described by several groups.[50,56,57] To test whether the ETS-ROS model can adequately capture this dependence, we compared the simulated J_{H2O2} to experimentally determined values at varying $[O_2]$. As shown, the model simulations are consistent with experimental data when mitochondria are energized with NADH-linked substrates and QH_2-linked substrates with RET inhibition. Further, the monotonic relationship between J_{H2O2} and $[O_2]$ is dependent on substrate utilization. In the S/R condition, the net J_{H2O2} is more sensitive to changes in $[O_2]$, and a non-linearity is observed at low $[O_2]$. Model analysis reveals this non-linearity is a manifestation of how mitochondrial produce hydrogen peroxide at the lower $[O_2]$ (Figure 5B). The rapid drop in hydrogen peroxide production as $[O_2]$ approaches zero is due to a decreased availability of the reduced I_{FMN}. In our model, flavin sites must be unoccupied before they are able to react with O_2. This occurs because of the following: first, the reduced I_{FMN} preferentially binds to NAD^+ over NADH.[38,58] Second, the kinetic pressures between NADH production (via residual ME activity) and NADH consumption (via ROS production reactions) results in a gradual but complete reduction of the NAD pool as the $[O_2]$ required for ROS production approaches zero. Consequently, the net J_{H2O2} vs $[O_2]$ is non-linear with the S/R combination which we will now explicitly show in the next section. A similar mechanism likely exists for the P/M condition, but our simplified, lumped Krebs cycle expression does not capture this phenomenon well. We anticipate that we will reproduce this relationship when the model is extended to include better a representation of the enzymatic processes in the Krebs cycle.

Model Predictions

The high level of consistency between model simulations and experimental data demonstrate that our model is structurally sound and appropriately calibrated. We next used the ETS-ROS model to (1) investigate the linear and non-linear relationship of $[O_2]$ on J_{H2O2}, (2) predict the effects of substrate utilization on site-specific and species-specific contributions to mitochondrial ROS production during different respiratory states and ETS flux directions, (3) assess the degree of mitochondrial scavenging activity and % utilization during the experimental conditions in the calibration and corroboration data sets, and (4) elucidate the impact on the rate of ROS emission of the redox states of the NAD and Q pools, along with the mitochondrial membrane potential. These model predictions provide valuable mechanistic information about mitochondrial redox homeostasis that are experimentally inaccessible.

Hydrogen Peroxide Production By Site I_F Underlies the Kinetics of Net ROS Emission Rates At Low $[O_2]$

Preliminary model analysis of the monotonic dependence between net J_{H2O2} and $[O_2]$ reveals that, when mitochondria are energized by succinate and RET is inhibited with rotenone, H_2O_2 production is non-linearly sensitive to changes in $[O_2]$ (Figure 5B). We previously explained this phenomenon with an
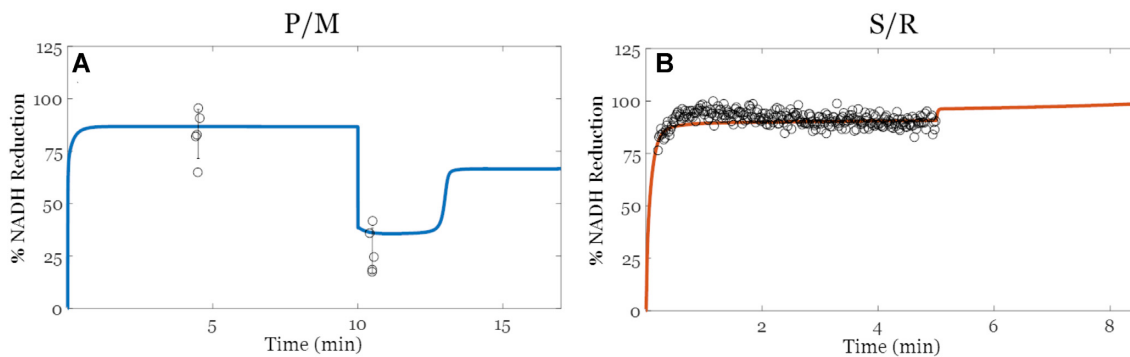
Figure 3. Model simulations of NADH reduction (%). (A) Pyruvate/L-malate (P/M). (B) Succinate with rotenone (S/R). The model outputs are represented by solid lines and within the experimental ranges. Individual data points are included; error bars represent the standard deviations. Experimental data are obtained using mitochondria isolated from the ventricular cardiomyocytes of guinea pigs. As shown, the model outputs are within the experimental ranges. Overall, succinate-supported respiration in the presence of rotenone maintains a more reduced NADH pool compared to P/M.
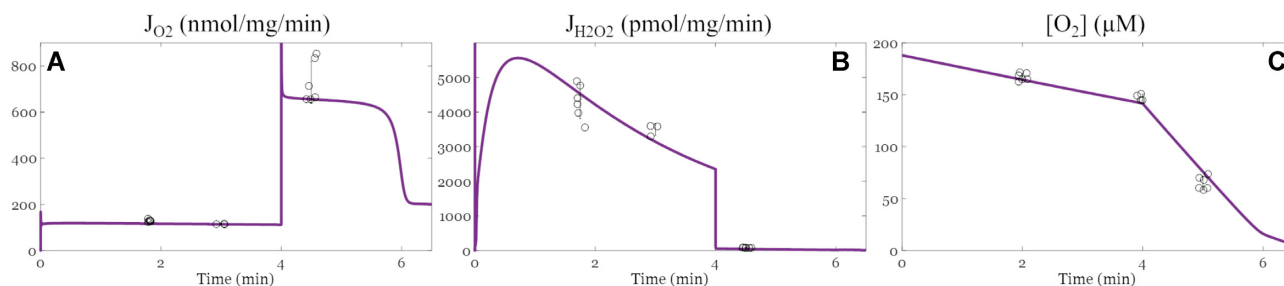

Figure 4. Model simulations of oxygen consumption rates (J_{O2}, nmol/mg/min), hydrogen peroxide emission rates (J_{H2O2}, pmol/mg/min) and oxygen concentration dynamics when the substrates include both pyruvate/L-malate (P/M) and succinate (S). The model outputs are represented by the solid lines. Individual data points are shown by the open black circles; error bars represent the standard deviations. Experimental data are obtained using mitochondria isolated from the ventricular cardiomyocytes of guinea pigs, as described in our previous work.[50] Isolated mitochondria (0.1 mg/mL) were energized with P/M/S. The respiratory and net hydrogen peroxide emission rates were quantified simultaneously using the O2k oxygraph.
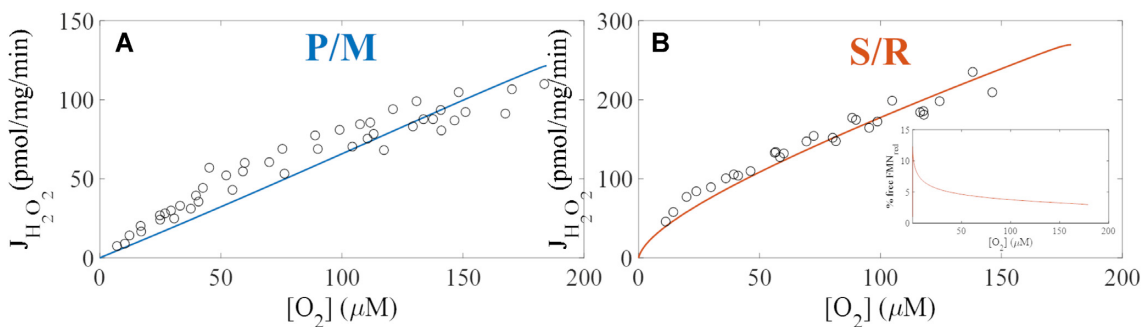

Figure 5. Model simulation of the monotonic relationship between net hydrogen peroxide emission rates (J_{H2O2}, pmol/mg/min) and oxygen concentrations (μM). Open, black circles represent experimental data. Model simulations are shown by the solid lines. Experimental data and simulated values were leak-state J_{H2O2} values at varying oxygen concentrations. (A) Mitochondria were energized with P/M. (B) Mitochondria were energized with S and RET is inhibited (S/R). As shown, the model is able to capture the monotonic dependence between J_{H2O2} and [O_2] for both substrates. Importantly, the monotonicity appears linear with P/M and non-linear with S/R as the substrates.

empirical model which was unable to identify redox center contributions to this behavior.[50] Using our computational ETS-ROS model, we dissected the individual processes underlying the net J_{H2O2} measurements as shown in Figure 6. Here, the total ROS (J_{ROS}) is defined with respect to 2-electron equivalents and equals the sum of hydrogen peroxide (J_{H2O2}) plus half of the superoxide flux ($J_{SO}/2$). The scavenging capacity shown in right y-axis of panels shown in Figure 6A and 6D reflect the fraction scavenging capacity utilization. In the P/M condition, the scavenging system activity is only a few % of the maximum rate of H_2O_2 clearance. In contrast, the scavenging system activity increases to 15% when mitochondria are energized with S/R.

This increase in scavenging activity is expected as mitochondria respiring in the S/R condition produce more ROS compared to the P/M condition (Figure 6A and 6D). This goes up even further when S or P/M/S are used as respiratory fuels, as we will show later. In the presence of P/M, a linear dependence between total J_{ROS} and [O_2] was observed, and H_2O_2 production is low (Figure 6A). However, J_{ROS} exhibit a non-linear dependence on [O_2] under S/R-supported respiration (Figure 6D). The primary reason for this difference is the H_2O_2 producing activity of the I_F site.

Regardless of the substrates, most H_2O_2 originates from the fully reduced flavin of complex I, which produces the non-linear
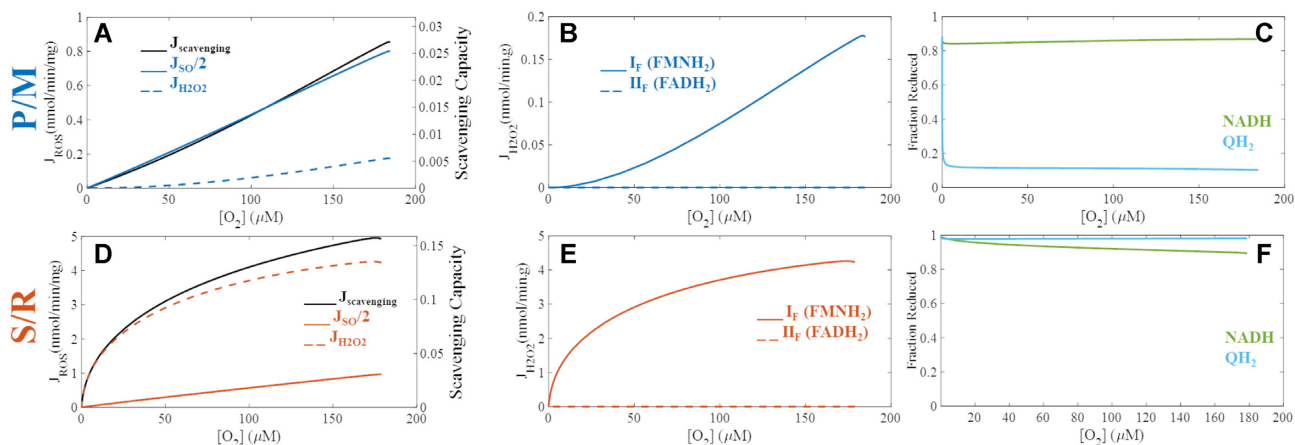
Figure 6. Model analysis of site-specific H_2O_2 production and bioenergetics variables critical to mitochondrial ROS production over a range of $[O_2]$ (μM). To further understand the substrate-specific monotonicity associated with the net J_{H2O2} on $[O_2]$ (Figure 5), model analysis was performed to extract additional mechanistic insights. The total ROS, superoxide and hydrogen peroxide fluxes are shown with active scavenging under P/M (A) and S/R (D) simulations. Total ROS flux (J_{ROS}, solid lines) is defined as the sum of hydrogen peroxide flux (J_{H2O2}, dotted lines) and half of the superoxide flux (J_{SO}, dashed lines). The fully reduced flavin of complex I contributes to most J_{H2O2} under both P/M- (B) and S/R- (E) supported respiration. It also underlies the non-linearity associated with J_{ROS} at low $[O_2]$ in the S/R simulation. The model further demonstrates that the redox states of the NADH and the Q pools are highly sensitive to experimental conditions (C and F). Rotenone inhibits QH_2 oxidation at site I_Q, which indirectly prevents effective NADH oxidation at site I_F. The NADH pool is, thus, significantly reduced in the S/R simulation, creating a condition conducive for H_2O_2 production.

relationship between J_{ROS} and $[O_2]$ for S/R supported respiration (Figure 6B and 6E). The combination of highly reduced NAD^+ and Q pools redox states explains the J_{H2O2} profile associated with each substrate combinations (Figure 6C and 6F). In the P/M simulation, the NADH pool is less reduced, and the Q pool is significantly oxidized. In contrast, rotenone in the S/R simulation prevents quinol oxidation at site I_Q and NADH oxidation at site I_F, maintaining the NADH and Q pools in mostly reduced states. As seen in Figure 6F, the NADH level at high $[O_2]$ is 90% reduced and rises to 100% as $[O_2]$ approaches zero. At high $[O_2]$, most of the reduced flavin is bound up with NAD^+ despite it being only 10% of the NAD^+ pool. This is because NAD^+ binds with about 10-fold higher affinity than NADH to the reduced flavin on complex I. However, as O_2 is depleted, the NAD^+ pool becomes progressively reduced freeing the binding site near the reduced flavin to maintain H_2O_2 production at elevated rates until anoxia (Figure 5B, inset).

Site-Specific Superoxide and Hydrogen Peroxide Production Rates
As shown in Figures 7 and 8, the site-specific contributions to total superoxide and hydrogen peroxide production are determined by substrate combinations, respiratory states, and ETS flux directions. The site-specific superoxide production rates are also shown in Table 5 whereas site-specific hydrogen peroxide production rates are included in the text below.

During leak state with substrate combinations favoring RET (S and P/M/S), ROS is produced primarily at sites I_Q and I_{FMNH2} (Figure 7A). The rates from these sites exceed 25 times that of the next highest site. When operating in FET mode, these two sites are joined by III_{Qp} as the top 3 ROS producers. In the S/R condition, sites I_Q and I_{FMNH2} are replaced by both CII sites as top ROS producers when their individual contributions are combined. Even so, I_{FMNH2} still produces ROS in this condition because the FMN on complex I is unobstructed in the presence of rotenone. Both complex II sites increase their individual ROS production rates due to the presence of a highly reduced Q pool. During oxphos, bioenergetic conditions are quite different and the mitochondrial redox couples become more oxidized, in general.

Figure 7B shows that the ROS production rates in the oxphos state from all sites are dramatically reduced with a similar profile relative to the leak state. Notably, sites I_Q and I_{FMNH2} remain the sites with the highest capacity to produce ROS. Despite high ETS turnover, complex I redox centers are maintained in a reduced state, producing high ROS emission rates. In the oxphos state, the NAD^+ pool becomes more oxidized, but the Q pool gets more reduced. This is due to the activation of parts of the tricarboxylic acid (TCA) cycle via metabolite and allosteric modulatory changes.[18] As a result, complex II and III sites do not significantly drop below leak-state rates despite a large drop in membrane potential and NADH levels. The high rates of sites I_Q and I_{FMNH2} in S and P/M/S conditions during the oxphos state is somewhat surprising. During leak state, the FMN of complex I is operating in a near-equilibrium state under highly reducing conditions. The I_Q site feeds electrons into the complex to support ROS production at both sites. In contrast, the sites at complex I are displaced from equilibrium during oxphos and contribute to electron flow down to O_2. Yet, in this state, these sites still produce ROS at a rate of around 5 times or more when compared to the other sites. The sites that produce H_2O_2 show a similar pattern.

As direct H_2O_2 production by the respiratory chain is a 2-electron redox reaction, only the I_{FMNH2} and II_{FADH2} are considered as ETS sources of H_2O_2 in the model. Regardless of respiratory states and substrate sources, almost all H_2O_2 produced by mitochondria originate from the I_{FMNH2} site (Figure 8). Site II_{FADH2} produces very little H_2O_2 in the presence of fumarate.[39] Transitioning to oxphos from leak state leads to a more dramatic reduction J_{H2O2} relative to J_{SO}. This is because J_{H2O2} relies more heavily on NADH rather than QH_2 or the membrane potential.[38,39] In the S/R condition, the mitochondrial NAD pool is more reduced relative to the P/M condition due to the (i) presence of ME activity and (ii) inhibition of complex I. Under S and P/M/S conditions, the model predicts that the hydrogen peroxide production rate from site I_{FMNH2} is similar. Consequently, most of the decrease in total hydrogen peroxide after the transition to oxphos results from decreased production by this site. However, phosphorylating mitochondria energized by P/M/S produce
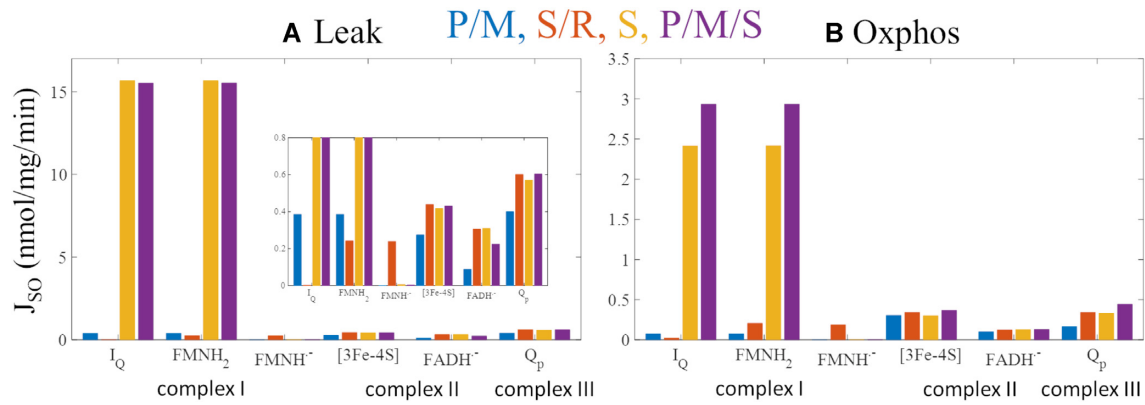
Figure 7. Model predictions of superoxide production at ETS redox centers in leak (A) and oxphos (B) states. In non-phosphorylating mitochondria (leak) energized with P/M or S/R, FET is favored whereas S and P/M/S favor RET. Complex I redox centers include the quinone reductase site (I_Q) and the FMN (I_{FMNH2} = reduced flavin mononucleotide, $I_{FMNH.-}$ = flavin mononucleotide radical). Complex II redox centers are the [3Fe-4S] cluster ($II_{[3Fe-4S]}$) and the FAD ($II_{FADH.-}$ = flavin adenine dinucleotide radical). The Q_p site resides in complex III (III_{Qp}). Overall, superoxide production is lowest under P/M-supported respiration and minimized by phosphorylation. The highly reduced Q pool and a high membrane potential under S- and P/M/S-supported respiration maintain sites I_Q and I_F in the highly reduced states regardless of respiratory states, favoring superoxide production by these sites I_Q and I_F and making complex I the greatest combined source of superoxide.
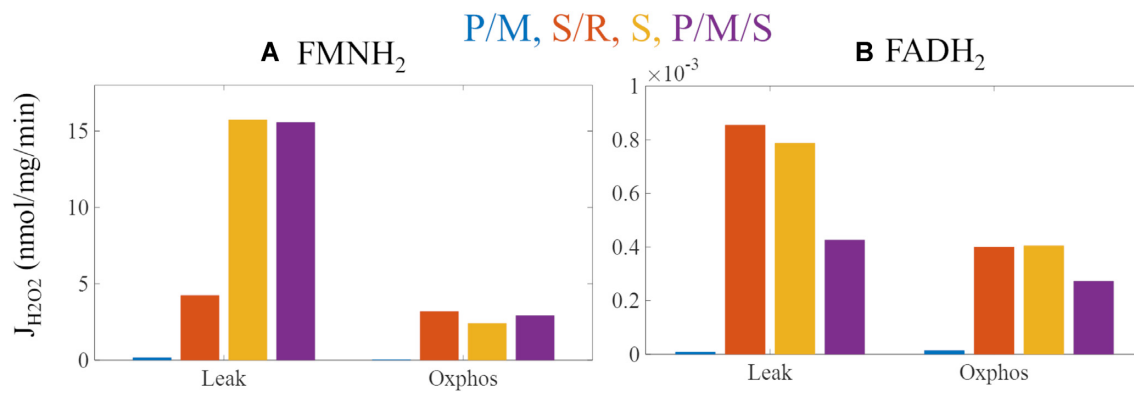

Figure 8. Model predictions of hydrogen peroxide production at ETS redox centers at leak (A) and oxphos (B) states. Only the I_{FMNH2} and II_{FADH2} are considered as hydrogen peroxide production requires 2 electrons. Left axis values are for I_{FMNH2}, and right axis values are for II_{FADH2}. In non-phosphorylating mitochondria energized with P/M or S/R, FET is favored whereas S and P/M/S favor RET. Overall, hydrogen peroxide production is lowest under P/M-supported respiration and minimized by phosphorylation, similar to superoxide production. Regardless of the respiratory states and electron flux directions, most hydrogen peroxide originates from the I_{FMNH2}.

Table 5. Model Predictions of Site-Specific Superoxide Production (J_{SO}, nmol/mg/min) During Leak and Oxphos States Supported by Different Substrates.

State	Leak				Oxphos			
Site/substrates	P/M	S/R	S	P/M/S	P/M	S/R	S	P/M/S
I_Q	0.395	0.003	15.7	15.6	0.046	0.019	1.87	2.22
I_{FMNH2}	0.395	0.244	15.7	15.6	0.046	0.209	1.87	2.22
$I_{FMNH.-}$	~0	0.241	0.006	0.004	~0	0.190	0.001	0.001
$II_{[3Fe-4S]}$	0.277	0.436	0.417	0.431	0.315	0.340	0.299	0.365
$II_{FADH.-}$	0.087	0.303	0.311	0.224	0.10	0.117	0.106	0.111
III_{Qp}	0.401	0.601	0.574	0.606	0.145	0.337	0.301	0.413

Values less than 10^{-4} are shown as ~0.

more hydrogen peroxide from the I_{FMNH2} site compared to S alone. In the P/M/S condition, pyruvate metabolism produces NADH through the TCA cycle which results in a more reduced NAD^+ pool. Consequently, the I_{FMNH2} site is more reduced under P/M/S-supported respiration, enhancing hydrogen peroxide arising from this site.

Effects of Substrate Utilization and Electron Transport Mode on Scavenging Activity

The activity of the scavenging systems' response to changes in ROS production remains an enigma for the same reasons that the origins of mitochondrial ROS under native conditions are inconclusive. Therefore, due to the lack of quantitative data, we modeled the scavenging system assuming that it is saturable
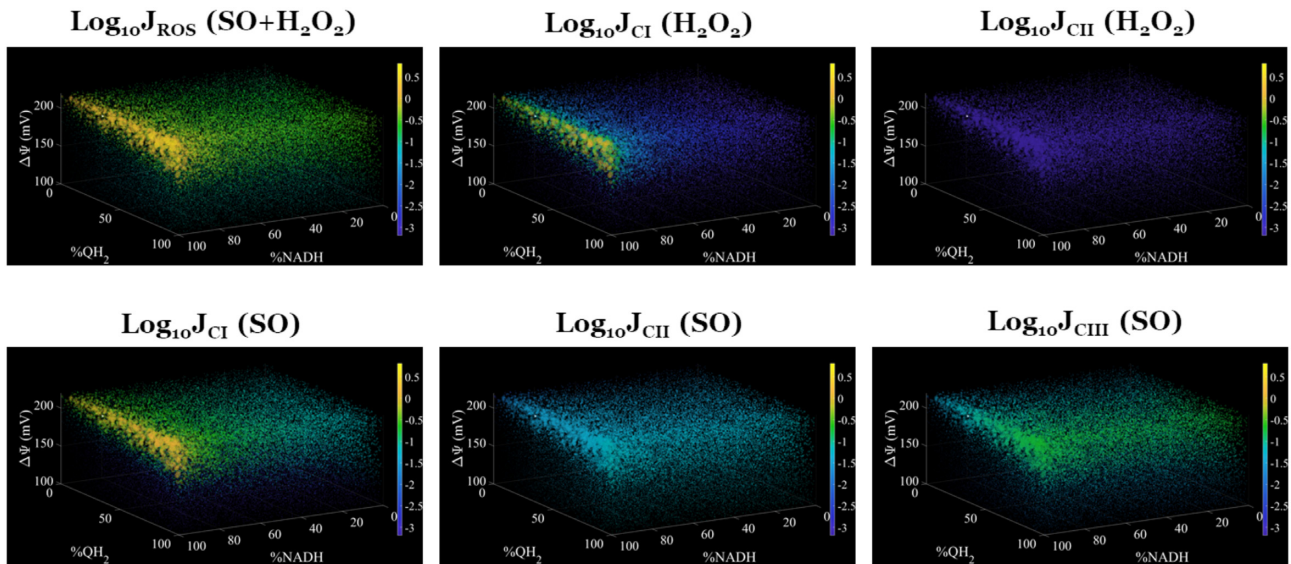
Figure 9. Model predictions of superoxide and hydrogen peroxide fluxes (J_{SO} and J_{H2O2}, respectively) from all and individual ETS complexes under P/M supported respiration. The state variables at 5-min steady state were fixed and the membrane potential ($\Delta\Psi$), %NADH, and %QH$_2$ were adjusted in the ranges shown. Model outputs are the $\log_{10}$ values of each flux with units of nmol/mg/min. Also, model outputs are represented as colored dots where the size of the dot is proportional to the model output's value relative to the colorbar. The white dot in each panel represents the starting point before adjusting $\Delta\Psi$, %NADH, and %QH$_2$.

and responsive to changes in matrix H$_2$O$_2$ production. To do so, we used a simple, lumped empirical Michaelis–Menten expression shown in Section 3 of the supplement. This expression consists of a V_{max} and a K_M term for H2O2 affinity which were fit to the data presented herein. Because regenerating the scavenging system relies on NAD(P)H, ROS scavenging has a limited capacity.[10] Thus, the responsive nature of the scavenging system to matrix H$_2$O$_2$ is necessary to keep net ROS production in the physiological range. In this model, these assumptions were adequate as the model outputs in the calibration and corroboration stages are consistent with experimental data. Thus, we used the model to predict the rate of ROS scavenging in the experimental conditions simulated in Figure 1. The model reveals that scavenging activity is lower in FET mode, which is unsurprising since it is consistent with lower ROS production. In RET mode, the scavenging activity is operating near maximum and ROS emission rates increase nearly 40-fold. Currently, the kinetic properties of the intact scavenging system remain a deep mystery. This is, in part, due to the complex biochemistry occurring in the mitochondrial matrix. For example, there is compelling evidence for a ROS-related substrate channeling system embedded in the matrix,[59] but the molecular details of this phenomena are still obscure. Thus, changes in scavenging capacity or H$_2$O$_2$ sensitivity can result in elevated ROS emission rates that will lead to cellular oxidative stress.

Primary Determinants of ROS Production

The corroborated model is further used to explore the effects of the mitochondrial membrane potential along with the NADH and Q pool redox state on J_{SO} and J_{H2O2} from individual complexes (Figure 9). In this simulation, we simulated the model until reaching the steady state with respect to mitochondrial state variables under the P/M condition. We clamped substrates at saturating levels and oxygen at a physiological level of 20 μM[10] in this simulation. We then perturbed the membrane potential, NAD$^+$ redox state, and Q pool redox state while keeping the

other state variables fixed and computed the resultant free radical fluxes. This simulation exemplifies the utility of model in testing hypotheses that are not experimentally feasible.

The model predicts a maximum rate of ROS production occurs when the membrane potential is high and the NAD$^+$ and Q pools are extremely reduced (Figure 9). In general, at high membrane potentials, mitochondrial ROS production is more sensitive to NADH levels than QH$_2$ levels. When NADH levels begin to exceed 90%, ROS production exponentially increases. That said, QH$_2$ levels still significantly affect total ROS production showing saturation at more oxidized levels. Of the H$_2$O$_2$ producing sites, complex I produces significantly more ROS compared to complex II. Its maxima lie along the 100% NADH and 220 mV membrane potential plane where QH$_2$ is maximally reduced. In contrast to the H$_2$O$_2$ producings sites, the rates of the SO producing sites are distributed differently. Complex I dominates in RET mode and contributes little to SO production under more oxidized conditions. Complex II produces the least amount of SO under these conditions and is independent of NADH. As expected from our prior study, complex II SO production is very sensitive to QH$_2$ levels. In contrast, complex III produces a moderate amount of SO and contributes to the basal level of SO production by the mitochondrial respiratory chain. As with the other ETS pumps, this complex produces most SO when the membrane potential, NADH levels, and QH$_2$ levels are high.

The ETS-ROS model was used to predict the bioenergetic response of mitochondria to an increase in adenosine triphosphate (ATP) demand for the substrate combinations use for calibration and corroboration. These results shown in Figure 10 reveal the respiratory dynamics, ROS emission profile, and dynamics of other bioenergetic variables encoded by the model follow expected behavior. With an increase in ATP demand, respiration monotonically increases until the max capacity of the ETS and oxphos-related processes are attained. At high demand, the ETS pumps are outcompeted by the adenine nucleotide translocase, inorganic phosphate carrier, and ATP synthase. Consequently, the membrane potential decreases in a
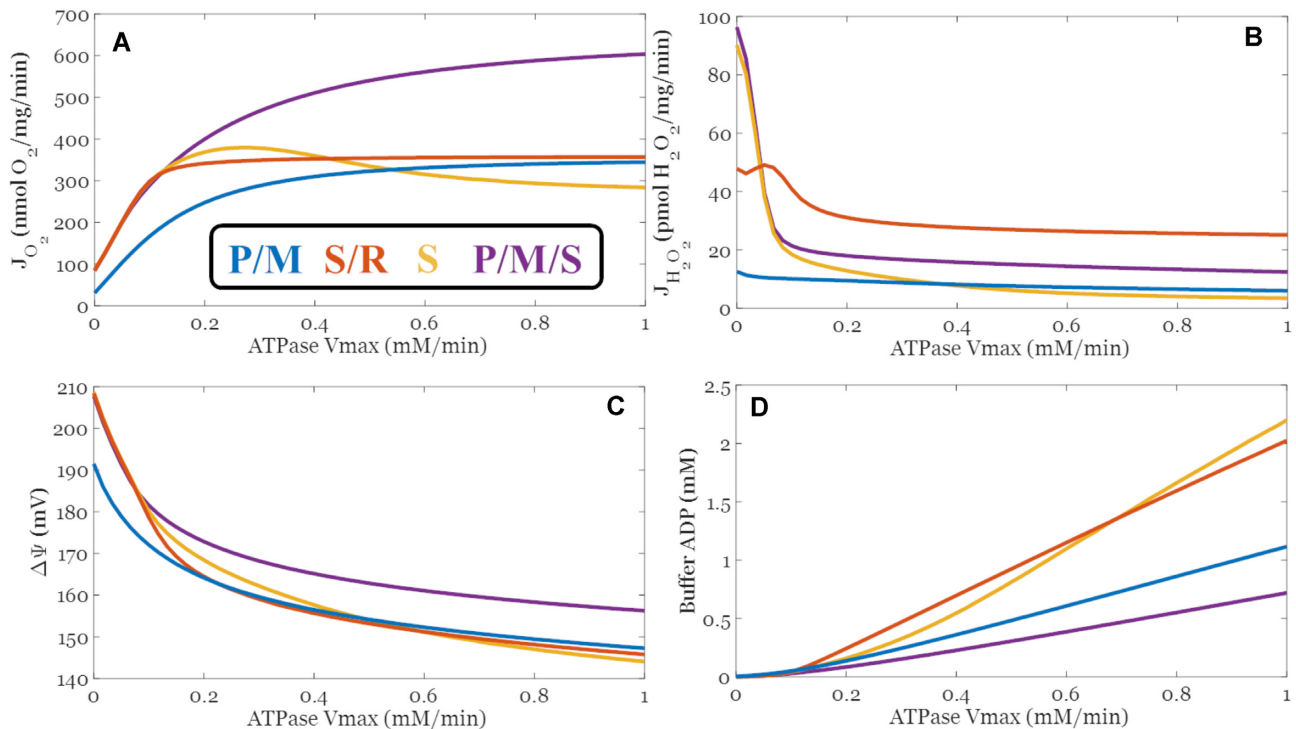
Figure 10. Select model outputs demonstrating the changes in key bioenergetic variables during changes in ATP demand. Model simulation protocols were like those used for simulating the experimental conditions presented in the accompanying article. The only major differences are the inclusion of 10 mM ATP in the extramitochondrial space as an initial condition, a more physiological O_2 concentration at 20 μM, and external metabolites, buffer pH, and O_2 were clamped. The model was then run out to a steady state at the ATPase Vmax's as shown on the x-axis. These simulation results are consistent with what we know about the impact of ATP-demand on respiration (A), ROS output (B), membrane potential (C), and extra-mitochondrial, steady-state ADP levels (D) for the given conditions. The decrease in the respiratory rate with succinate as ATP demand increases is due to OAA inhibition.

titratable manner. As a corollary, mitochondrial ROS emission is decreased. Due to the relative membrane potential independent kinetics of succinate dehydrogenase, the S/R condition results in the fastest ROS emission rate when ATP demand is high. What is also revealed by these simulations is the ability of mitochondria to defend against ATP demand when substrate supply is ample and diverse. This notion is reflected in the membrane potential and extra-mitochondrial ADP concentrations. The P/M/S combination resulted in the highest membrane potential and the lowest ADP concentration profile among all combinations. A strong dependence on the membrane potential for ROS output is reflected in the 5-fold drop of ROS emission rates when the membrane potential decreases only about 10% (~20 mV). Figures S2 and S3 show Figure 10 results plotted against ATPase rate instead of Vmax. The plots look quantitatively different because our ATPase expression (given in Section 3 of the supplement) encodes an ADP-dependent negative feedback mechanism we developed to represent external ATPases in our experiments.[18] In addition, we explored the role succinate plays on enhancing energy production and ROS emission at sub-saturating pyruvate (100 μM) and malate concentrations (0.5 mM) in the presence of moderate ATP demand (~50% of max). The results shown Figure S4 reveal that as succinate levels are increased, there is a corresponding increase in respiration, ROS emission, membrane potential, and % reduced redox pools (NADH, QH_2, and cyt c) with a concomitant decrease in extra-mitochondrial ADP. The lower ADP levels are a direct consequence of increasing the membrane potential that enables the generation of stronger phosphorylation potentials (~[ATP]/[ADP]/[Pi]). Each

of these results demonstrate the model's ability to characterize bioenergetic changes associated with energy demand and support its general utility. That said, these results should be interpreted with care until the model is validated after the addition of other major matrix enzymes and transporters involved in energy metabolism.

Discussion

Model Predictions of Site-Specific ROS From the ETS Complexes

Site-specific ROS production has inspired many experimental studies and led to a wealth of experimental data. However, the data are limited to experimental conditions wherein inhibitors are present. The use of different systems, experimental conditions, and techniques has also led to discrepancies among these studies. Simpler systems, such as purified enzymes, have the advantage that fewer variables need to be accounted for in interpreting experimental results. But the conclusions may not be applicable when these results are integrated into biochemical reaction networks. On the contrary, a more intact system affords an environment more similar to in vivo conditions but introduces more hidden variables. Perhaps the biggest hidden variable in all mitochondrial studies is the dynamic redox state of the Q pool. There is currently no experimental method that can be used to quantify the real-time dynamic changes of the Q pool without sample destruction. Additionally, factors that affect thermodynamics such as temperature, buffer ionic
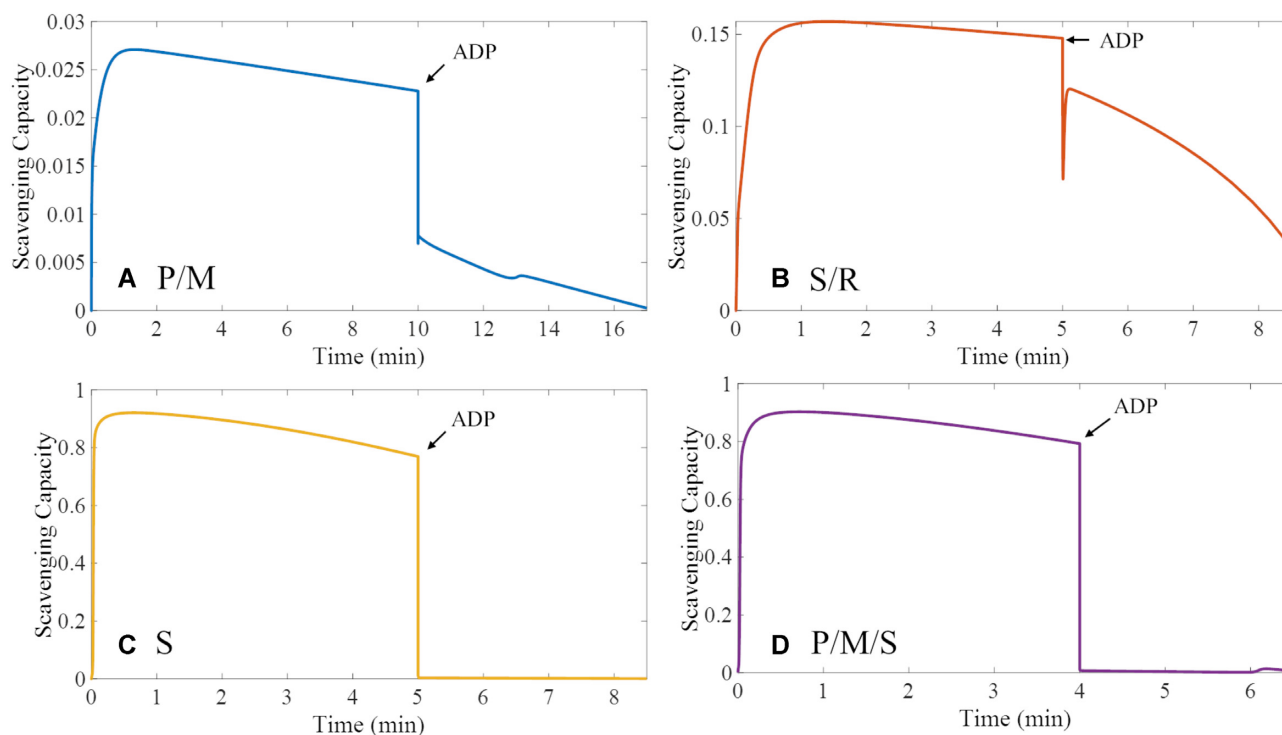
Figure 11. Model predictions of active scavenging under different metabolic conditions. FET occurs under P/M- and S/R-supported respiration (A, B). RET occurs under S- and P/M/S-supported respiration (C, D). ADP addition results in maximal oxidative phosphorylation (oxphos state). During oxphos, the scavenging activity decreases regardless of the electron source and transport mode. Under RET mode, the scavenging activity is significantly increased but unable to keep the net J_{H2O2} at comparable levels to under FET. The model predictions of active scavenging, thus, together with the changes in J_{H2O2} and membrane potential support the assumptions that the scavenging activity is saturable and responds to changes in ROS production.

strength, and buffer pH can all regulate enzyme activities but are often neglected. These changes can lead to large changes in pathway fluxes and study outcomes. A computational approach can be applied to fully realize unified analyses at high temporal and spatial resolutions. Thus, different experimental conditions are analyzed using a unified framework to reconcile contradictory reports. This quantitative framework not only checks for the internal consistency of data but also enables extrapolation to experimentally untestable space for hypothesis testing or generation.

While detailed computer models of mitochondrial metabolism have been around since the 1970s,[60–66] there are only a few that integrate ROS homeostasis with substrate metabolism.[18,35,41,42,46,67] For an overview of these models, the review by Mazat et al. is an excellent source.[68] These models each have their own unique strengths and focuses, but the current ETS-ROS model is distinguished from these prior models in several important ways. First, complexes I, II, and III are included as sources of ROS while prior models only included I and/or III. As this study demonstrates, ROS from complex II is not insignificant, and is produced at high rates under the right circumstances. So, to quantitatively ascribe ROS production rates to each complex, all three major ROS producing sites are required. Second, the ETS-ROS model includes mechanisms required to simulate the dynamic range between low (leak) and high (oxphos) flux regimes. Not all prior models possess this ability without requiring parameter or structural changes. In the ETS-ROS model, the metabolite concentration profiles control electron flow through the ETS. This type of behavior is desirable when extrapolating up to more complex systems. And

third, the core elements of the ETS-ROS model are coded up to ensure thermodynamic consistency. This feature is shared by some models and keeps model behavior within the feasible biochemical reaction space, and it strengthens the utility of multi-scale models. In any case, each of these models are extremely useful in aiding our ability to understand the general features of mitochondrial ROS metabolism.

Using the ETS-ROS model, we identify the ROS species and their origin (Figures 8 and 11) under the different metabolic conditions of our experimental data (Figure 2). We found that the III_{Qp} site, site I_{FMNH2}, and site I_Q as a semiquinone are the primary sources of superoxide in non-phosphorylating mitochondria energized with P/M (Figure 7 and Table 5). In non-phosphorylating mitochondria, site $I_{FMNH^{\cdot -}}$ gives rise to a considerable amount of superoxide under QH_2-supported respiration when RET is inhibited (S/R). These model predictions reconcile experimental results regarding complex I from different studies. For example, Galkin and Brandt[30] and Grivennikova and Vinogradov[29] independently concluded that both the fully reduced flavin (FMNH$_2$) and the flavin radical (FMNH$^-$) can give rise to superoxide. Kussmaul and Hirst also found that site I_F is a primary source of superoxide but only when fully reduced.[28] In contrast, Lambert and Brand reported that site I_Q is the predominant source of superoxide originating from Complex I.[21] The Ohnishi group found that both sites I_Q and I_F are ROS sources when they exist in the radical forms.[31] Thus, computational modeling shows that the differences among experimental data are likely due to different experimental conditions and that even seemingly contradictory results may be true under the right conditions.

Like complex I, the identity and origin of ROS produced by complex II remain unresolved. Until recently, it was thought to be a negligible source of mitochondrial ROS. Quinlan et al. found that site II$_F$ produces comparable amounts of ROS to site I$_Q$ in the presence of fatty acids.[20] The notion that site II$_F$ produces most ROS from complex II is shared by Siebels and Drose.[34] However, others contend that significant amounts of ROS originate from the site II$_Q$ [69] and the ISC near the Q site.[70] We used the model to identify conditions that favor ROS production by complex II and the contributions of its redox centers. In particular, the model identifies site II$_{[3Fe-4S]}$ as the primary source of superoxide arising from complex II. In FET, superoxide arising from site II$_{FADH}$ becomes more significant only under QH$_2$-supported respiration (S/R). Thus, our model supports the experimental results that the ISC near the Q site and site II$_F$ give rise to most of complex II's ROS. Moreover, the model predicts that FET in non-phosphorylating mitochondria favors superoxide production by complex III. The bc1 complex also contributes significantly to total superoxide flux in phosphorylating mitochondria although its contribution is more pronounced in FET mode. Unfortunately, all these predictions remain difficult to experimentally test due to the lack of a robust, quantitative, and straight-forward method to directly measure them without interfering with other processes.

An interesting theory relevant to this study is the concept of a partitioned or segmented Q pool. In the early days of the bioenergetics field, evidence against Q pool segmentation was provided with the aid of computer modeling.[71–74] These earlier studies are supported by more recent experimental evidence.[75] However, with the advent of new molecular and genetic tools, there has been a renewed interest in this theory.[76–79] These new data compel further research into this phenomenon. Based on the available evidence at this time, an integrated model is likely required to support evidence for or against this idea. It is quite possible that Q pool segmentation is a unique phenomenon associated with specific physiological circumstances that control cristae and inner membrane arrangement or that specific cells and tissues are wired with sufficient differences to observe this condition. Currently, the ETS-ROS model is unable to test this theory in its present form, but we believe the ETS-ROS model can be extended to test this theory.

Next Steps for Expanding the ETS-ROS Model to Include More ROS-Related Pathways

In developing this model, we focused on the known primary sources of mitochondrial ROS, the ETS complexes. Electron flavoprotein,[80–82] dihydrolipoamide dehydrogenase,[15,16,83] and other mitochondrial dehydrogenases[84,85] are additional sources of ROS that may become significant in different physiological conditions and tissues. In the next evolution of the ETS-ROS model, we will expand the model to include 2 major modifications. The first is to expand the model to explicitly include the full TCA cycle with additional enzymatic processes uncovered during the development of this model (eg, ME). This requires additional experiments to collect data on metabolite profiles under the various conditions. Second, we will develop models of beta-oxidation that are able to simulate both kinetic turnover and ROS production from electron flavoprotein and other associated ROS processes. This will, again, require additional experiments focused on fatty acid metabolism under various conditions spanning across the anticipated physiological domain.

Lastly, we will revisit the scavenging system to include glutathione and thioredoxin scavenging enzymes in addition to NAD(P) transhydrogenase. Despite the high level of consistency between model simulations and experimental data (Figures 2–5), this approach is incapable of partitioning the roles of the glutathione and thioredoxin systems involved in the ROS detoxifying pathway. Addressing these aspects require additional experimental data under the prevailing conditions to properly calibrate the model. Individual kinetic models of each of the four primary enzymes responsible for most of the H$_2$O$_2$ scavenging are already developed, but they remain untested in an integrated model.[86–88] In all cases, each future generation of the model will be more refined and enable testing of hypotheses that are experimentally infeasible.

Conclusions

In conclusion, we have developed, analyzed, and corroborated a model of mitochondrial ROS that identifies the species-specific ROS originating from the ETS redox centers under varying respiratory states and electron flux directions. Each ROS-producing module is constructed in a thermodynamically faithful manner and tested prior to being unified in a single platform.[38–40] The biophysical details included in the model are supported by experimental data and further refined by the process of sensitivity analysis. Being modular, parsimonious, and consistent, this modeling approach enables the individual modules within the model to work harmoniously with each other in a thermodynamically faithful manner. This approach also facilitates the inclusion of other mitochondrial physiology processes that are related to ROS homeostasis, as mentioned above, when data become available. These qualities distinguish this model from existing models which also attempt to recapitulate mitochondrial ROS homeostasis[41,42] as ours is capable of consistently reproducing experimental data on various aspects of mitochondrial physiology and making predictions that are physiologically relevant.

Supplementary Material

Supplementary material is available at the *APS Function* online.

Abbreviations

The abbreviations used are: SDH, succinate dehydrogenase; ROS, reactive oxygen species; ISC, iron sulfur center; SQ, semiquinone; O$_2^{\bullet-}$, superoxide; H$_2$O$_2$, hydrogen peroxide; I/R, ischemia/reperfusion; PMS, phenazine methosulfate; TMPD, N, N, N', N'-tetramethyl-p-phenylenediamine.

Author Contributions

Concept and design: JNB and QVD. Acquisition of data: JNB, QVD, MJD, JOSR, and YL. Analysis and interpretation of data: JNB, QVD, and YL. Development of computer code: JNB and QVD. Drafting or revising the article: JNB, QVD, and YL.

Data Availability

All data, model equations, and model codes described in this manuscript are given in the main body or supplement.

References

1. Garlid AO, Jaburek M, Jacobs JP, Garlid KD. Mitochondrial reactive oxygen species: which ROS signals cardioprotection? *Am J Physiol Heart Circ Physiol*. 2013;**305**(7):H960–H968. doi:10.1152/ajpheart.00858.2012.

2. Sena LA, Li S, Jairaman A, et al. Mitochondria are required for antigen-specific T cell activation through reactive oxygen species signaling. *Immunity*. 2013;**38**(2):225–236. doi:10.1016/j.immuni.2012.10.020.

3. Zhang Y, Choksi S, Chen K, Pobezinskaya Y, Linnoila I, Liu ZG. ROS play a critical role in the differentiation of alternatively activated macrophages and the occurrence of tumor-associated macrophages. *Cell Res*. 2013;**23**(7):898–914. doi:10.1038/cr.2013.75.

4. Padgett LE, Burg AR, Lei W, Tse HM. Loss of NADPH oxidase-derived superoxide skews macrophage phenotypes to delay type 1 diabetes. *Diabetes*. 2015;**64**(3):937–946. doi:10.2337/db14-0929.

5. Yellon DM, Hausenloy DJ. Myocardial reperfusion injury. *N Engl J Med*. 2007;**357**(11):1121–1135. doi:10.1056/NEJMra071667.

6. Jaeschke H, Woolbright BL. Current strategies to minimize hepatic ischemia-reperfusion injury by targeting reactive oxygen species. *Transplant Rev*. 2012;**26**(2):103–114. doi:10.1016/j.trre.2011.10.006.

7. Gutierrez G, Reines HD, Wulf-Gutierrez ME. Clinical review: hemorrhagic shock. *Critical Care*. 2004;**8**(5):373–381. doi:10.1186/cc2851.

8. Ibanez B, Heusch G, Ovize M, Van de Werf F. Evolving therapies for myocardial ischemia/reperfusion injury. *J Am Coll Cardiol*. 2015;**65**(14):1454–1471. doi:10.1016/j.jacc.2015.02.032.

9. Heusch G, Gersh BJ. The pathophysiology of acute myocardial infarction and strategies of protection beyond reperfusion: a continual challenge. *Eur Heart J*. 2017;**38**(11):774–784. doi:10.1093/eurheartj/ehw224.

10. Murphy MP. How mitochondria produce reactive oxygen species. *Biochem J*. 2009;**417**(1):1–13. doi:10.1042/BJ20081386.

11. Muller F. The nature and mechanism of superoxide production by the electron transport chain: its relevance to aging. *J Am Aging Assoc*. 2000;**23**(4):227–253. doi:10.1007/s11357-000-0022-9.

12. Ambrosio G, Zweier JL, Duilio C, et al. Evidence that mitochondrial respiration is a source of potentially toxic oxygen free radicals in intact rabbit hearts subjected to ischemia and reflow. *J Biol Chem*. 1993;**268**(25):18532–18541. https://www.ncbi.nlm.nih.gov/pubmed/8395507. Published 1993/09/05.

13. Andreyev AY, Kushnareva YE, Starkov AA. Mitochondrial metabolism of reactive oxygen species. *Biochemistry (Moscow)*. 2005;**70**(2):200–214. doi:10.1007/s10541-005-0102-7.

14. Adam-Vizi V, Chinopoulos C. Bioenergetics and the formation of mitochondrial reactive oxygen species. *Trends Pharmacol Sci*. 2006;**27**(12):639–645. doi:10.1016/j.tips.2006.10.005.

15. Starkov AA, Fiskum G, Chinopoulos C, et al. Mitochondrial alpha-ketoglutarate dehydrogenase complex generates reactive oxygen species. *J Neurosci*. 2004;**24**(36):7779–7788. doi:10.1523/JNEUROSCI.1899-04.2004.

16. Tretter L, Adam-Vizi V. Generation of reactive oxygen species in the reaction catalyzed by alpha-ketoglutarate dehydrogenase. *J Neurosci*. 2004;**24**(36):7771–7778. doi:10.1523/JNEUROSCI.1842-04.2004.

17. Bunik VI, Sievers C. Inactivation of the 2-oxo acid dehydrogenase complexes upon generation of intrinsic radical species. *Eur J Biochem*. 2002;**269**(20):5004–5015. doi:10.1046/j.1432-1033.2002.03204.x.

18. Bazil JN, Beard DA, Vinnakota KC. Catalytic coupling of oxidative phosphorylation, ATP demand, and reactive oxygen species generation. *Biophys J*. 2016;**110**(4):962–971. doi:10.1016/j.bpj.2015.09.036.

19. Chouchani ET, Pell VR, James AM, et al. A unifying mechanism for mitochondrial superoxide production during ischemia-reperfusion injury. *Cell Metab*. 2016;**23**(2):254–263. doi:10.1016/j.cmet.2015.12.009.

20. Quinlan CL, Perevoschikova IV, Goncalves RL, Hey-Mogensen M, Brand MD. The determination and analysis of site-specific rates of mitochondrial reactive oxygen species production. *Methods Enzymol*. 2013;**526**:189–217. doi:10.1016/B978-0-12-405883-5.00012-0.

21. Lambert AJ, Brand MD. Inhibitors of the quinone-binding site allow rapid superoxide production from mitochondrial NADH:ubiquinone oxidoreductase (complex I). *J Biol Chem*. 2004;**279**(38):39414–39420. doi:10.1074/jbc.M406576200.

22. Hirst J. Mitochondrial complex I. *Annu Rev Biochem*. 2013;**82**(1):551–575. doi:10.1146/annurev-biochem-070511-103700.

23. Wirth C, Brandt U, Hunte C, Zickermann V. Structure and function of mitochondrial complex I. *Biochim Biophys Acta*. 2016;**1857**(7):902–914. doi:10.1016/j.bbabio.2016.02.013.

24. Sun F, Huo X, Zhai Y, et al. Crystal structure of mitochondrial respiratory membrane protein complex II. *Cell*. 2005;**121**(7):1043–1057. doi:10.1016/j.cell.2005.05.025.

25. Yankovskaya V, Horsefield R, Tornroth S, et al. Architecture of succinate dehydrogenase and reactive oxygen species generation. *Science*. 2003;**299**(5607):700–704. doi:10.1126/science.1079605.

26. Crofts AR. The cytochrome bc1 complex: function in the context of structure. *Annu Rev Physiol*. 2004;**66**(1):689–733. doi:10.1146/annurev.physiol.66.032102.150251.

27. Ksenzenko M, Konstantinov AA, Khomutov GB, Tikhonov AN, Ruuge EK. Effect of electron transfer inhibitors on superoxide generation in the cytochrome bc1 site of the mitochondrial respiratory chain. *FEBS Lett*. 1983;**155**(1):19–24. doi:10.1016/0014-5793(83)80200-2.

28. Kussmaul L, Hirst J. The mechanism of superoxide production by NADH:ubiquinone oxidoreductase (complex I) from bovine heart mitochondria. *Proc Natl Acad Sci*. 2006;**103**(20):7607–7612. doi:10.1073/pnas.0510977103.

29. Grivennikova VG, Vinogradov AD. Generation of superoxide by the mitochondrial Complex I. *Biochim Biophys Acta*. 2006;**1757**(5-6):553–561. doi:10.1016/j.bbabio.2006.03.013.

30. Galkin A, Brandt U. Superoxide radical formation by pure complex I (NADH:ubiquinone oxidoreductase) from Yarrowia lipolytica. *J Biol Chem*. 2005;**280**(34):30129–30135. doi:10.1074/jbc.M504709200.

31. Ohnishi ST, Shinzawa-Itoh K, Ohta K, Yoshikawa S, Ohnishi T. New insights into the superoxide generation sites in bovine heart NADH-ubiquinone oxidoreductase (Complex I): the significance of protein-associated ubiquinone and the dynamic shifting of generation sites between semiflavin and semiquinone radicals. *Biochim Biophys Acta*. 2010;**1797**(12):1901–1909. doi:10.1016/j.bbabio.2010.05.012.

32. St-Pierre J, Buckingham JA, Roebuck SJ, Brand MD. Topology of superoxide production from different sites in the mitochondrial electron transport chain. *J Biol Chem*. 2002;**277**(47):44784–44790. doi:10.1074/jbc.M207217200.

33. Quinlan CL, Orr AL, Perevoshchikova IV, Treberg JR, Ackrell BA, Brand MD. Mitochondrial complex II can generate reactive oxygen species at high rates in both the forward and reverse reactions. *J Biol Chem*. 2012;**287**(32):27255–27264. doi:10.1074/jbc.M112.374629.

34. Siebels I, Drose S. Q-site inhibitor induced ROS production of mitochondrial complex II is attenuated by TCA cycle dicarboxylates. *Biochim Biophys Acta*. 2013;**1827**(10):1156–1164. doi:10.1016/j.bbabio.2013.06.005.

35. Selivanov VA, Votyakova TV, Zeak JA, Trucco M, Roca J, Cascante M. Bistability of mitochondrial respiration underlies paradoxical reactive oxygen species generation induced by anoxia. *PLoS Comput Biol*. 2009;**5**(12):e1000619. doi:10.1371/journal.pcbi.1000619.

36. Korzeniewski B, Zoladz JA. A model of oxidative phosphorylation in mammalian skeletal muscle. *Biophys Chem*. 2001;**92**(1-2):17–34. doi:10.1016/s0301-4622(01)00184-3.

37. Chen X, Qi F, Dash RK, Beard DA. Kinetics and regulation of mammalian NADH-ubiquinone oxidoreductase (Complex I). *Biophys J*. 2010;**99**(5):1426–1436. doi:10.1016/j.bpj.2010.06.063.

38. Bazil JN, Pannala VR, Dash RK, Beard DA. Determining the origins of superoxide and hydrogen peroxide in the mammalian NADH:ubiquinone oxidoreductase. *Free Radic Biol Med*. 2014;**77**:121–129. doi:10.1016/j.freeradbiomed.2014.08.023.

39. Manhas N, Duong QV, Lee P, et al. Computationally modeling mammalian succinate dehydrogenase kinetics identifies the origins and primary determinants of ROS production. *J Biol Chem*. 2020;**295**(45):15262–15279. doi:10.1074/jbc.RA120.014483.

40. Bazil JN. Analysis of a functional dimer model of ubiquinol cytochrome c oxidoreductase. *Biophys J*. 2017;**113**(7):1599–1612. doi:10.1016/j.bpj.2017.08.018.

41. Gauthier LD, Greenstein JL, O'Rourke B, Winslow RL. An integrated mitochondrial ROS production and scavenging model: implications for heart failure. *Biophys J*. 2013;**105**(12):2832–2842. doi:10.1016/j.bpj.2013.11.007.

42. Gauthier LD, Greenstein JL, Cortassa S, O'Rourke B, Winslow RL. A computational model of reactive oxygen species and redox balance in cardiac mitochondria. *Biophys J*. 2013;**105**(4):1045–1056. doi:10.1016/j.bpj.2013.07.006.

43. Demin OV, Kholodenko BN, Skulachev VP. A model of O2.-generation in the complex III of the electron transport chain. *Mol Cell Biochem*. 1998;**184**(1/2):21–33. https://www.ncbi.nlm.nih.gov/pubmed/9746310.

44. Ransac S, Arnarez C, Mazat JP. The flitting of electrons in complex I: a stochastic approach. *Biochim Biophys Acta*. 2010;**1797**(6-7):641–648. doi:10.1016/j.bbabio.2010.03.011.

45. Bleier L, Drose S. Superoxide generation by complex III: from mechanistic rationales to functional consequences. *Biochim Biophys Acta*. 2013;**1827**(11-12):1320–1331. doi:10.1016/j.bbabio.2012.12.002.

46. Markevich NI, Hoek JB. Computational modeling analysis of mitochondrial superoxide production under varying substrate conditions and upon inhibition of different segments of the electron transport chain. *Biochim Biophys Acta*. 2015;**1847**(6-7):656–679. doi:10.1016/j.bbabio.2015.04.005.

47. Brdiczka D, Pette D. Intra- and extramitochondrial isozymes of (NADP) malate dehydrogenase. *Eur J Biochem*. 1971;**19**(4):546–551. doi:10.1111/j.1432-1033.1971.tb01347.x.

48. Nolte J, Brdiczka D, Pette D. Intracellular distribution of phosphoenolpyruvate carboxylase and (NADP) malate dehydrogenase in different muscle types. *Biochim Biophys Acta*. 1972;**284**(2):497–507. doi:10.1016/0005-2744(72)90148-9.

49. Tsai CS. Spontaneous decarboxylation of oxalacetic acid. *Can J Chem*. 1967;**45**(8):873–880. doi:10.1139/v67-145.

50. Duong QV, Hoffman A, Zhong K, Dessinger MJ, Zhang Y, Bazil JN. Calcium overload decreases net free radical emission in cardiac mitochondria. *Mitochondrion*. 2020;**51**:126–139. doi:10.1016/j.mito.2020.01.005.

51. Wollenman LC, Vander Ploeg MR, Miller ML, Zhang Y, Bazil JN. The effect of respiration buffer composition on mitochondrial metabolism and function. *PLoS One*. 2017;**12**(11):e0187523. doi:10.1371/journal.pone.0187523.

52. Malyala S, Zhang Y, Strubbe JO, Bazil JN. Calcium phosphate precipitation inhibits mitochondrial energy metabolism. *PLoS Comput Biol*. 2019;**15**(1):e1006719. doi:10.1371/journal.pcbi.1006719.

53. Vinogradov AD, Kotlyar AB, Burov VI, Belikova YO. Regulation of succinate dehydrogenase and tautomerization of oxaloacetate. *Adv Enzyme Regul*. 1989;**28**:271–280. doi:10.1016/0065-2571(89)90076-9.

54. Okun JG, Lummen P, Brandt U. Three classes of inhibitors share a common binding domain in mitochondrial complex I (NADH:ubiquinone oxidoreductase). *J Biol Chem*. 1999;**274**(5):2625–2630. doi:10.1074/jbc.274.5.2625.

55. Gnaiger E, Aasander FE, Abdul KN, et al. Mitochondrial respiratory states and rates. *Bioenerg Commun*. 2020;**1**. doi:10.26124/bec:2020-0001.v1.

56. Robb EL, Hall AR, Prime TA, et al. Control of mitochondrial superoxide production by reverse electron transport at complex I. *J Biol Chem*. 2018;**293**(25):9869–9879. doi:10.1074/jbc.RA118.003647.

57. Hoffman DL, Brookes PS. Oxygen sensitivity of mitochondrial reactive oxygen species generation depends on metabolic conditions. *J Biol Chem*. 2009;**284**(24):16236–16245. doi:10.1074/jbc.M809512200.

58. Vinogradov AD. NADH/NAD+ interaction with NADH: ubiquinone oxidoreductase (complex I). *Biochim Biophys Acta*. 2008;**1777**(7-8):729–734. doi:10.1016/j.bbabio.2008.04.014.

59. Wagner M, Bertero E, Nickel A, et al. Selective NADH communication from alpha-ketoglutarate dehydrogenase to mitochondrial transhydrogenase prevents reactive oxygen species formation under reducing conditions in the heart. *Basic Res Cardiol*. 2020;**115**(5):53. doi:10.1007/s00395-020-0815-1.

60. Kohn MC, Garfinkel D. Computer simulation of metabolism in palmitate-perfused rat heart. I. Palmitate oxidation. *Ann Biomed Eng*. 1983;**11**(5):361–384. doi:10.1007/BF02584214.

61. Kohn MC, Garfinkel D. Computer simulation of metabolism in palmitate-perfused rat heart. II. Behavior of complete model. *Ann Biomed Eng*. 1983;**11**(6):511–531. doi:10.1007/BF02364082.

62. Achs MJ, Kohn MC, Garfinkel D. Computer simulation of metabolism in pyruvate-perfused rat heart. IV. Model behavior. *Am J Physiol*. 1979;**237**(3):R174–180. doi:10.1152/ajpregu.1979.237.3.R174.

63. Kohn MC, Achs MJ, Garfinkel D. Computer simulation of metabolism in pyruvate-perfused rat heart. III. Pyruvate dehydrogenase. *Am J Physiol*. 1979;**237**(3):R167–173. doi:10.1152/ajpregu.1979.237.3.R167.

64. Kohn MC, Achs MJ, Garfinkel D. Computer simulation of metabolism in pyruvate-perfused rat heart. I.

Model construction. *Am J Physiol*. 1979;**237**(3):R153–158. doi:10.1152/ajpregu.1979.237.3.R153.

65. Garfinkel D, Kohn MC, Achs MJ. Computer simulation of metabolism in pyruvate-perfused rat heart. V. Physiological implications. *Am J Physiol*. 1979;**237**(3):R181–186. doi:10.1152/ajpregu.1979.237.3.R181.

66. Kohn MC, Achs MJ, Garfinkel D. Computer simulation of metabolism in pyruvate-perfused rat heart. II. Krebs cycle. *Am J Physiol*. 1979;**237**(3):R159–166. doi:10.1152/ajpregu.1979.237.3.R159.

67. Kembro JM, Aon MA, Winslow RL, O'Rourke B, Cortassa S. Integrating mitochondrial energetics, redox and ROS metabolic networks: a two-compartment model. *Biophys J*. 2013;**104**(2):332–343. doi:10.1016/j.bpj.2012.11.3808.

68. Mazat JP, Devin A, Ransac S. Modelling mitochondrial ROS production by the respiratory chain. *Cell Mol Life Sci*. 2020;**77**(3):455–465. doi:10.1007/s00018-019-03381-1.

69. Paranagama MP, Sakamoto K, Amino H, Awano M, Miyoshi H, Kita K. Contribution of the FAD and quinone binding sites to the production of reactive oxygen species from Ascaris suum mitochondrial complex II. *Mitochondrion*. 2010;**10**(2):158–165. doi:10.1016/j.mito.2009.12.145.

70. Grivennikova VG, Kozlovsky VS, Vinogradov AD. Respiratory complex II: ROS production and the kinetics of ubiquinone reduction. *Biochim Biophys Acta*. 2017;**1858**(2):109–117. doi:10.1016/j.bbabio.2016.10.008.

71. Kroger A, Klingenberg M. Further evidence for the pool function of ubiquinone as derived from the inhibition of the electron transport by antimycin. *Eur J Biochem*. 1973;**39**(2):313–323. doi:10.1111/j.1432-1033.1973.tb03129.x.

72. Ragan CI, Cottingham IR. The kinetics of quinone pools in electron transport. *Biochim Biophys Acta*. 1985;**811**(1):13–31. doi:10.1016/0304-4173(85)90003-5.

73. Reed JS, Ragan CI. The effect of rate limitation by cytochrome c on the redox state of the ubiquinone pool in reconstituted NADH: cytochrome c reductase. *Biochem J*. 1987;**247**(3):657–662. doi:10.1042/bj2470657.

74. Crofts AR, Meinhardt SW, Jones KR, Snozzi M. The role of the quinone pool in the cyclic electron-transfer chain of *Rhodopseudomonas sphaeroides*: a modified Q-Cycle mechanism. *Biochim Biophys Acta*. 1983;**723**(2):202–218. doi:10.1016/0005-2728(83)90120-2.

75. Blaza JN, Serreli R, Jones AJ, Mohammed K, Hirst J. Kinetic evidence against partitioning of the ubiquinone pool and the catalytic relevance of respiratory-chain supercomplexes. *Proc Natl Acad Sci*. 2014;**111**(44):15735–15740. doi:10.1073/pnas.1413855111.

76. Kayser EB, Sedensky MM, Morgan PG, Hoppel CL. Mitochondrial oxidative phosphorylation is defective in the long-lived mutant clk-1. *J Biol Chem*. 2004;**279**(52):54479–54486. doi:10.1074/jbc.M403066200.

77. Turunen M, Olsson J, Dallner G. Metabolism and function of coenzyme Q. *Biochim Biophys Acta*. 2004;**1660**(1-2):171–199. doi:10.1016/j.bbamem.2003.11.012.

78. Calvo E, Cogliati S, Hernansanz-Agustin P, et al. Functional role of respiratory supercomplexes in mice: SCAF1 relevance and segmentation of the Qpool. *Sci Adv*. 2020;**6**(26):eaba7509. doi:10.1126/sciadv.aba7509.

79. Hernansanz-Agustin P, Enriquez JA. Functional segmentation of CoQ and cyt c pools by respiratory complex superassembly. *Free Radic Biol Med*. 2021;**167**:232–242. doi:10.1016/j.freeradbiomed.2021.03.010.

80. Cornelius N, Byron C, Hargreaves I, et al. Secondary coenzyme Q10 deficiency and oxidative stress in cultured fibroblasts from patients with riboflavin responsive multiple Acyl-CoA dehydrogenation deficiency. *Hum Mol Genet*. 2013;**22**(19):3819–3827. doi:10.1093/hmg/ddt232.

81. Perevoshchikova IV, Quinlan CL, Orr AL, Gerencser AA, Brand MD. Sites of superoxide and hydrogen peroxide production during fatty acid oxidation in rat skeletal muscle mitochondria. *Free Radic Biol Med*. 2013;**61**:298–309. doi:10.1016/j.freeradbiomed.2013.04.006.

82. Seifert EL, Estey C, Xuan JY, Harper ME. Electron transport chain-dependent and -independent mechanisms of mitochondrial H2O2 emission during long-chain fatty acid oxidation. *J Biol Chem*. 2010;**285**(8):5748–5758. doi:10.1074/jbc.M109.026203.

83. Quinlan CL, Goncalves RL, Hey-Mogensen M, Yadava N, Bunik VI, Brand MD. The 2-oxoacid dehydrogenase complexes in mitochondria can produce superoxide/hydrogen peroxide at much higher rates than complex I. *J Biol Chem*. 2014;**289**(12):8312–8325. doi:10.1074/jbc.M113.545301.

84. Forman HJ, Kennedy J. Dihydroorotate-dependent superoxide production in rat brain and liver. A function of the primary dehydrogenase. *Arch Biochem Biophys*. 1976;**173**(1):219–224. doi:10.1016/0003-9861(76)90252-6.

85. Tretter L, Takacs K, Hegedus V, Adam-Vizi V. Characteristics of alpha-glycerophosphate-evoked H2O2 generation in brain mitochondria. *J Neurochem*. 2007;**100**(3):650–663. doi:10.1111/j.1471-4159.2006.04223.x.

86. Pannala VR, Dash RK. Mechanistic characterization of the thioredoxin system in the removal of hydrogen peroxide. *Free Radic Biol Med*. 2015;**78**:42–55. doi:10.1016/j.freeradbiomed.2014.10.508.

87. Pannala VR, Bazil JN, Camara AK, Dash RK. A mechanistic mathematical model for the catalytic action of glutathione peroxidase. *Free Radic Res*. 2014;**48**(4):487–502. doi:10.3109/10715762.2014.886775.

88. Pannala VR, Bazil JN, Camara AKS, Dash RK. A biophysically based mathematical model for the catalytic mechanism of glutathione reductase. *Free Radic Biol Med*. 2013;**65**:1385–1397. doi:10.1016/j.freeradbiomed.2013.10.001.